DISSERTATION

EXPERIMENTAL INVESTIGATION OF LASER-IGNITED HYDROCARBON SPRAYS AND DROPLETS

Submitted by:

Parneeth Lokini

Department of Mechanical Engineering

In partial fulfillment of the requirements

For the Degree of Doctor of Philosophy

Colorado State University

Fort Collins, Colorado

Summer 2025

Doctoral Committee:

Advisor: Azer P. Yalin
Co-advisor: Bret C. Windom

Ciprian Dumitrache
Alan Van Orden

ABSTRACT

EXPERIMENTAL INVESTIGATION OF LASER-IGNITED HYDROCARBON SPRAYS AND DROPLETS

Spray ignition involves complex multiphase interactions wherein atomized fuel droplets undergo evaporation, secondary breakup, and mixing with the oxidizer. These processes result in highly heterogeneous fuel-air mixtures, characterized by significant local equivalence ratio variations, complicating the establishment of consistent and reliable ignition conditions. Additionally, substantial energy losses occur in spray ignition, as a considerable portion of the input energy is consumed by droplet heating and vaporization rather than directly contributing to plasma formation and flame kernel initiation. The presence of turbulence further exacerbates ignition challenges by introducing local velocity gradients and strain that distort or extinguish nascent flame kernels. This dissertation aims to bridge the existing knowledge gaps in spray ignition through systematic experimental investigations under realistic yet controlled laboratory conditions. The research is structured into two complementary components: (1) laser-droplet interactions and droplet breakup dynamics, and (2) laser ignition of fuel sprays.

In the first component, experiments focus on elucidating how laser pulse energy and droplet size influence droplet fragmentation dynamics, plasma formation, and species evolution in the breakdown region. Utilizing diagnostics such as shadowgraphy and Laser-Induced Breakdown Spectroscopy (LIBS), droplet breakup regimes, species composition, electron densities, and temperatures are characterized. A novel energy-based metric is developed to effectively distinguish and classify different droplet fragmentation regimes. The experiments demonstrated that low laser energy densities (<~70 mJ/mm^3), designated as regime 1, resulted in a single plasma

breakdown event accompanied by broadband emission and C_2 Swan bands, suggesting weak plasma formation. Conversely, high energy densities (>~70 mJ/mm³), designated as regime 2, resulted in multiple plasma breakdowns that resulted in emission of H_α, O, and N, implying a full laser breakdown in the gaseous reactive mixture.

The second component includes laser ignition experiments that were performed in a heptane spray using an Nd:YAG laser to investigate its ignitability. In the first set, Laser-Induced Breakdown Spectroscopy (LIBS) and imaging were employed to quantify H_α/O ratios, kernel size, and kernel number at various locations within the spray. While these parameters generally followed the spray profile, they did not reliably predict ignition. In the second set, OH chemiluminescence, LIBS, and high-speed imaging was utilized to understand the effect of laser energy and ignition location on ignitability. Two distinct modes of ignition failure—short and long—were identified based on kernel extinction time. For the spray conditions studied, ignition was achieved at laser energy of 250 mJ, while long-mode failure occurred at 80 mJ, and short-mode failure at 30 mJ. Optical intensities of OH and CH showed that higher laser energies generated more radical species and sustained the flame long enough to establish stable ignition. Additionally, kernel trajectories extracted from high-speed images showed that ignition is more probable for cases where the spark is generated in or moves into recirculation zone. These findings enhance our understanding of spray ignitability and can inform the development and validation of models for laser or plasma-assisted combustion in sprays.

The results presented in this dissertation not only advance the fundamental understanding of spray ignition phenomena but also contribute toward the development of more reliable and efficient ignition systems. The broader significance of this research lies in its direct applicability to practical combustion systems, particularly aero-turbines where dependable ignition and stable flame

propagation are essential for safe and efficient operation. Moreover, the insights gained from this work can guide future experimental studies and enhance computational modeling efforts in the field of multiphase ignition.

ACKNOWLEDGMENTS

I would first like to express my sincere gratitude to Dr. Yalin for giving me the opportunity to pursue my Ph.D. When I started, I had no prior experience with lasers or optics, and his support throughout—from designing experiments and interpreting data to writing manuscripts and preparing for conferences—was instrumental in my growth as a researcher.

I am deeply grateful to Dr. Windom for teaching me how to enjoy the process of research and for encouraging a systematic approach to solving problems. His mentorship has had a lasting impact on the way I think and work. I also want to thank Dr. Dumitrache for always asking thoughtful, challenging questions and for instilling in me the importance of attention to detail. I am thankful to Dr. Van Orden for taking the time to serve on my committee and providing valuable feedback, and to Dr. Marchese for his guidance and support during some of the more difficult phases of my Ph.D. journey.

My time at the Powerhouse Energy Campus was made truly special by the people I had the privilege of working with. I am thankful to all the incredible friends and colleagues who not only contributed to my research but also made the lab a place I looked forward to coming to—even on Monday mornings. While the list is by no means exhaustive, I would especially like to thank my lab mates, past and present: Carter, Puga, Seth, Jacob, Jon, Brian, Manav, Miguel, and Reece. I'm also grateful to friends —Siddhesh, Mozhdeh, Arturo, Felipe, Tolu, Derek, Dan, Athul, Sanket, Projit, Nagarjun—for their camaraderie and encouragement.

Finally, I want to express my heartfelt appreciation to my parents and my brothers. Thank you for your unwavering love, patience, and support throughout these years. I truly could not have done this without you.

TABLE OF CONTENTS

CHAPTER 1:Introduction

1.1 Motivation

Ignition of a combustible mixture[1] refers to the initiation of a self-sustaining chemical reaction in a fuel–oxidizer system, typically triggered by an external energy source such as a spark plug or a laser. Successful ignition requires supplying sufficient energy to elevate a localized region—typically comparable to the laminar flame thickness—to the adiabatic flame temperature[1]. This process marks the transition from a chemically stable mixture to rapid combustion, releasing heat and forming reactive intermediates that result in the formation of a self-sustaining flame. Understanding and controlling ignition is critical for designing reliable ignition systems in practical combustion devices, including internal combustion engines and aero-turbines. These systems must achieve consistent ignition across a wide range of pressures, temperatures, and altitudes. Efficient ignition strategies can also reduce ignition delays, enable leaner combustion, and lower pollutant emissions. The broader significance of ignition research lies in its direct relevance to real-world combustion applications, where reliable ignition and stable flame holding are essential for safe and efficient operation. Despite its importance to engines, propulsion, and fire safety, ignition remains challenging to study due to its highly transient nature, sensitivity to initial conditions, and the complex coupling of fluid dynamics, chemical kinetics, and energy deposition[2].

Several factors influence the ignition process and one of the primary factors is the fuel–air ratio[1,2], which governs both the stability of the flame and the amount of heat released during combustion. Mixtures near the stoichiometric ratio generally exhibit more favorable ignition characteristics, while lean or rich mixtures may require higher ignition energies and may be more prone to

quenching. Initial temperature[1] is another critical parameter: higher temperatures promote faster chemical reaction rates, enhance radical production, and shorten ignition delay times, thereby increasing the likelihood of forming a stable flame. The presence of a radical-rich environment[1,2], particularly species such as H, O, and OH, further enhances ignition probability by accelerating chain-branching reactions that sustain combustion. Turbulence and local flow dynamics[2,3] also play a dual role. On one hand, turbulence can promote mixing, enhance heat and mass transfer and assist ignition by distributing hot radicals and reactants. On the other hand, strong velocity gradients or excessive strain can quench nascent flame kernels by enhancing heat loss or disrupting the flame structure. While these parameters are relatively well understood and more easily controlled in gaseous mixtures, ignition in sprays presents additional complexities.

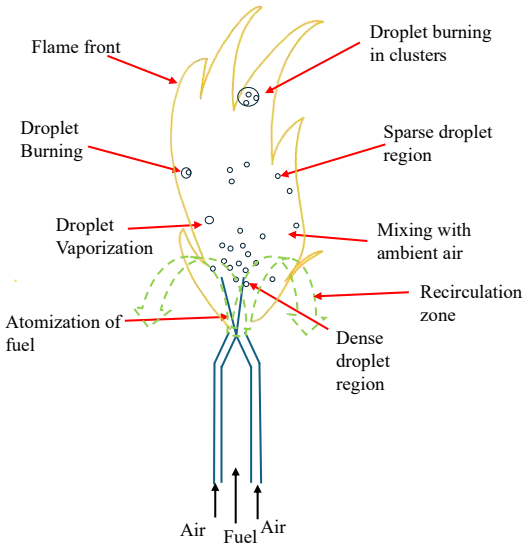

Figure 1.1 Illustration of Liquid Fuel Injection and Spray Combustion

Most of the challenges in studying ignition in spray systems stem from their inherently multiphase nature. Figure 1.1 illustrates the multiphase nature and the inherent inhomogeneity present in sprays. The presence of dispersed liquid droplets introduces substantial spatial heterogeneity in fuel–air mixing, resulting in locally varying equivalence ratios[4,5] and mixture reactivity. Non-

uniform droplet size distributions and vaporization rates further exacerbate this heterogeneity, often leading to fuel-rich or fuel-lean pockets that influence ignition kernel formation and flame propagation[6]. Moreover, droplet evaporation consumes a portion of the deposited energy[7,8], thereby reducing the amount available for ignition. In addition to thermal effects, droplets can optically interact with the ignition source either by scattering, absorbing, or focusing the incident energy[9,10] altering local energy densities through lensing effects[9]. The interaction between the spray momentum, background flow field, and turbulence adds another layer of complexity. The local velocity gradients[11] and strain rates[12] can either enhance ignition by promoting radical mixing or suppress it by increasing convective heat losses and kernel deformation.

In summary, spray ignition is inherently complex due to the combined effects of multiphase flow phenomena, stochastic plasma-droplet interactions, spatially inhomogeneous mixtures, and turbulence-driven flame kernel distortion. This study seeks to systematically address these challenges. Given that droplet interactions with the ignition source can critically influence ignition behavior, the first part of this research focuses on investigating these interactions in detail. Building on this foundation, the research will progress to ignition studies in a practical spray burner, aiming to better understand and isolate the specific challenges and mechanisms highlighted thus far. To enable a more precise and controlled experimental framework, a laser is employed as the ignition source in place of a traditional spark plug. Compared to spark ignition, laser-based ignition offers several advantages, including non-intrusive operation, flexible control over ignition timing and location, and reduced maintenance. The remainder of this chapter provides a detailed review of prior studies on laser–droplet interactions to understand droplet behavior in sprays, followed by a discussion on the ignition of spray systems, culminating in the formulation of the research objectives.

1.2 Literature Review

1.2.1 Laser interaction with droplets

Numerous research groups have investigated the interaction between laser plasmas and liquid droplets[13–28]. Eickmans et al.[29] conducted laser-induced breakup studies on freely falling water droplets (diameter ~ 100 μm) and demonstrated that laser intensity significantly influences droplet breakup. Depending on the intensity, the resulting plume may contain droplet fragments on one side or symmetrically on both sides of the original droplet. Hsieh et al.[20] implemented laser breakdown experiments on water droplets in an argon atmosphere. Spectroscopic analysis revealed that the plasma generated inside the droplet emits a broadband continuum, while emissions from either side of the droplet exhibit both continuum and discrete spectral lines from neutral and ionized species. While both of these studies were among the first to investigate droplet fragmentation, they offered limited control over experimental conditions, as the droplets were freely falling. Moreover, their study was restricted to water droplets only.

Klein et al.[13] studied the fragmentation of water droplets (diameter ~1mm) induced by a nanosecond laser, aiming to uncover the underlying physics of droplet breakup. Both laser energy and laser profile were found to influence the type of breakup. The study identified two Rayleigh-Taylor instabilities of different origins as the primary mechanisms driving the fragmentation. Avila et al.[16] studied the fragmentation of levitated water droplets (diameter ~0.2-1.5 mm) induced by cavitation bubbles. They established three fragmentation regimes based on laser energy and droplet size, namely, atomization, sheet formation, and coarse fragmentation. More recently Jagadale et al.[30] established different fragmentation regimes in diesel droplets(diameter ~100 μm) by laser-induced bubbles using multiple femtosecond laser pulses. While these studies employed a more

controlled setup using a levitator to suspend a single droplet and successfully established distinct fragmentation regimes, their focus remained limited to the fluid mechanical aspects of breakup. Rao et al.[15] investigated the laser-induced fragmentation of water and diesel droplets (diameter ~0.2-0.4 mm) in an array, employing shadowgraphy techniques. They established that the droplet surface acts as a lens and therefore, the actual formation of the laser spark inside the droplet may not be similar to the location of focus of laser beam. Furthermore, it was found that the breakdown of the droplet can be a single mode breakdown, or a multi-mode breakdown, based on the location of the laser focus. Bulat et. al[19] developed models to study the interaction of laser pulse with droplets. They also posited various stages of optical breakdown of the droplet as shown in Figure 1.3. When the laser beam is focused inside the droplet, super heating of the liquid occurs where the temperature exceeds the temperature of the saturated vapor at a given temperature. This leads to the formation of an internal vapor cavity shown in Figure 1.3a, also referred to as a cavitation bubble, inside the droplet. The subsequent absorption of laser pulse increases the pressure in the vapor cavity resulting in the formation of plasma which generates a shock wave as shown in Figure 1.3 d. The shock wave at later times results in the breakup of the droplets into smaller fragments as shown in Figures 1.3f. Again, while these studies provided valuable insights into the droplet breakup regimes, they did not address the nature of the chemical species generated during breakdown, nor did they examine the temperature within these regions. Both of these parameters are critical determinants of the combustibility of a mixture, as they directly influence ignition potential, flame stability, and subsequent chemical reactions.

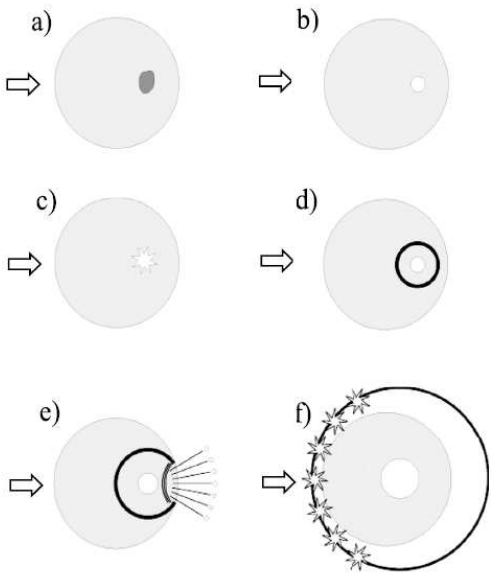

Figure 1.3 Mechanism of laser induced breakdown in a droplet.[19]

1.2.2 Forced Ignition in Gases and Sprays

Lewis and von Elbe[31] conducted experiments in methane–air mixtures and demonstrated that the characteristic size of the ignition source—specifically, the gap between electrodes in spark plug ignition—significantly influences the ignition probability. The required ignition energy increases when the characteristic size exceeds the optimal ignition kernel size (usually close to flame thickness), as this results in heating a larger volume of mixture than is optimal for ignition. Conversely, when the spark gap is smaller than the optimal ignition kernel size, the required energy also increases, because energy is confined to a smaller volume, leading to higher peak temperatures and greater radiative heat losses from the gas, as well as conductive heat losses to the electrodes. In contrast, for laser-induced spark ignition, this limitation is mitigated due to the absence of electrodes. The laser allows for electrode-free energy deposition, minimizing conductive heat loss and enabling precise spatial control over the ignition kernel size. Wienberg and Wilson[32] conducted experiments with a Q-switched ruby laser in methane-air mixtures and found that the

energy required for a laser is lower for very lean or very rich mixtures compared to spark ignition. Phuoc and White[33] further investigated ignition behavior using laser-induced spark ignition in a diffusion jet flames, examining ignition probability as a function of ignition location. They found that once the laser pulse energy exceeds the threshold required to ensure 100% gas breakdown probability, further increases in energy do not alter the spatial distribution of ignition probability. Instead, this spatial variation was primarily governed by local fluctuations in the fuel–air ratio, as well as variations in turbulence intensity and velocity gradients at the ignition site—factors that strongly affect local ignition conditions. While several other studies[3,34–42] have examined ignition in gaseous mixtures, the multiphase nature of sprays introduces additional complexities, and the insights from gaseous systems may not directly apply in spray ignition scenarios.

Nevertheless, numerous research groups have explored various aspects of spray ignition using both experimental and diagnostic approaches[4–6,9,37,42–54]. Kawahara et al.[9] conducted high-speed imaging of isooctane-air mixtures ignited by a laser-induced plasma. They explored the effect of microlensing caused by the droplets, where the curvature of the droplet changes the focus of the incoming laser beam, a result also observed in droplet studies by Rao et al.[15] However, they did not establish any contributing factors to ignitability of the spray. Marchione et al.[11] investigated the ignition of turbulent, swirling n-heptane spray flames using both single and multiple spark discharges. They identified several key factors that promote successful ignition, including spark placement within regions of negative axial velocity, relatively small droplet Sauter mean diameters (SMD ~20–50 μm), and mean equivalence ratios near stoichiometric conditions. The study distinguished between initial kernel generation and subsequent successful flame propagation and stabilization, emphasizing the critical role of kernel movement into regions capable of sustaining combustion. However, they relied solely on ignition probability as the ignition metric. While this

is useful, it does not directly reveal the influence of chemical kinetics—such as the presence of specific reactive species or temperature—or the effects of flow-field dynamics. Gebel et al.[45] also employed laser-induced breakdown spectroscopy (LIBS)[55,56] to investigate the transition from laser-induced breakdown plasma to flame kernel formation in kerosene sprays. Additionally, the appearance of radicals such as CN, C_2, and CH signaled the onset of combustion chemistry during the early stages of flame kernel development. However, the study did not attempt to establish a direct correlation between the observed species and the ignitability of the spray, limiting its ability to inform predictive ignition metrics.

Several studies have also categorized spray ignition behavior by identifying distinct failure modes, thereby offering a structured framework to understand flame kernel evolution and extinction dynamics. Mastorakos[6] proposed a three-phase model of spray ignition (1) flame kernel generation, (2) kernel/flame growth, and (3) flame stabilization. A successful ignition event requires avoiding quenching during these phases, from kernel formation to flame propagation, while events that lead to quenching and inhibit flame formation are nuanced and multifaceted. By examining ignition and extinction timescales, multiple failure modes have been identified to enhance the understanding of spray ignition and quenching dynamics. Oliveira et al.[4] characterized these failure modes based on the time relative to the spark. In *short-mode failure* quenching occurs shortly after ignition (<~0.5ms) as the kernel fails to grow sufficiently to sustain a flame. Conversely, in *long-mode failure* the kernel grows into a larger structure but is ultimately quenched by large-scale flow effects, preventing it from anchoring near the injector. To further distinguish these modes, they employed OH chemiluminescence imaging and LIBS[55–57] to analyze atomic emissions (H, O, N) and molecular species (CN, C_2) under various spray conditions and plasma

sizes. However, their study did not establish a direct correlation between the observed reactive species and ignition success or the failure modes.

1.3 Dissertation objectives

The current work aims to address critical gaps identified in the literature pertaining to both droplet dynamics and spray ignition. As mentioned earlier, previous studies have primarily focused on the fluid mechanical aspects of droplet fragmentation. Those that examined the species present in the plasma breakdown region often used water droplets (not fuel droplets) in freely falling configurations, where control over experimental conditions was limited. Notably, there has been little to no effort to quantify key plasma parameters—such as temperature and electron density—in realistic fuel droplet scenarios. Yet, these parameters could play a critical role in determining the ignitability of sprays. Therefore, the first component of this research aims to advance our understanding of droplet breakup dynamics by examining how laser pulse energy and droplet size influence the interaction and subsequent fragmentation and the species resulting from the breakdown. Using shadowgraphy imaging, the droplet breakup and associated plasma formation resulting from laser-droplet interaction were characterized. To further investigate the breakdown process, Laser-Induced Breakdown Spectroscopy (LIBS) was employed to analyze the resulting species and quantify plasma parameters such as electron density and temperature. In particular, spatially resolved LIBS was implemented by referencing LIBS spectra to the corresponding imaging data, enabling spatial mapping of breakdown locations and plasma characteristics across the interaction domain.

These fundamental insights into laser-induced droplet fragmentation provide a necessary foundation for extending the investigation to more complex multiphase systems. While the single-droplet study enables control over individual parameters and sheds light on the physical processes

governing laser energy deposition and plasma formation, real-world ignition environments like gas turbine combustors involve turbulent sprays with dense droplet regions, fluctuating equivalence ratios, and strong convective flows. To bridge this gap and build upon the findings of the droplet study, the second component of this research focuses on laser ignition of fuel sprays.

Some of the gaps identified in the literature pertain to the role of reactive species in influencing ignition, as well as the impact of flame kernel characteristics—such as size, number, and spatial distribution—on flame stability. Additionally, the influence of flow-field dynamics on both ignition and subsequent flame propagation remains largely unexplored. To elucidate the roles of chemical kinetics and flow-field dynamics in determining spray ignitability experiments were conducted by varying the ignition location within the spray to study the influence of local equivalence ratio on ignition outcomes. LIBS was used to measure the H/O atomic intensity ratio as a qualitative indicator of local equivalence ratio. Additionally, the number and size of flame kernels were quantified to explore how kernel statistics affect ignition success. Furthermore, by varying laser pulse energy and ignition location, three distinct ignition outcomes were observed: short-mode failure, long-mode failure, and successful ignition. These modes were distinguished based on the flame kernel's extinction timescale, as captured through high-speed imaging. LIBS was also used to detect emission from combustion-relevant radicals such as OH and CH. High-speed imaging not only enabled visualization of flame kernel evolution but also helped quantify kernel trajectories. Together, these diagnostics offer a comprehensive framework to interpret ignition behavior and predict failure modes. The results from this study pave the way for the development of closed-loop feedback systems to optimize ignition parameters and contribute to the broader goal of designing reliable and efficient ignition systems for spray combustion.

Additionally, the insights gained here can inform future experimental investigations and computational modeling efforts in multiphase laser ignition research.

This dissertation is organized as follows. Chapter 1 introduces the motivation behind the study and provides a comprehensive review of the existing literature on laser ignition of gases and sprays. Chapter 2 describes the experimental methodology, and the optical diagnostic setups employed throughout the research. Chapter 3 presents the experimental investigation of laser and droplet interaction, with a focus on droplet breakup and plasma formation. Chapter 4 discusses the results of laser-ignited spray combustion experiments, highlighting ignition behavior under varying conditions. Finally, Chapter 5 concludes the dissertation by summarizing the key findings, drawing overall conclusions, and outlining directions for future work.

CHAPTER 2:Theory and Methods[1]

This chapter provides an introduction to the fundamental theory of laser-induced plasma generation and its underlying mechanisms. It also describes the Laser-Induced Breakdown Spectroscopy (LIBS) diagnostic technique, which is extensively employed throughout this dissertation. The remainder of the chapter details the optical setups, experimental methods, and test conditions used in both the laser–droplet interaction study and the laser ignition of spray study.

2.1 Laser Induced Plasma Generation

A laser-induced plasma[51–53] is produced by focusing a laser beam with sufficient intensity to cause excitation and ionization of the molecules present in the region. Two primary ionization mechanisms lead to plasma formation and growth: multiphoton ionization (MPI) and electron avalanche ionization (EAI). The different stages of laser induced breakdown are shown in Figure 2.1. Multiphoton ionization[54,55] (as shown in Figure 2.1a) involves the absorption of several photons by a gas molecule and its subsequent ionization when the total energy of absorbed photons is larger than the ionization potential of the molecule. The MPI reaction can be described as follows:

$$M + nh\nu \rightarrow M^+ + e^- \tag{2.1}$$

[1] This chapter is based primarily on material published as a journal article: Lokini P, Dumitrache C, Windom BC, Yalin AP. Laser-Induced Breakdown Spectroscopy and Shadowgraphy of Acoustically Levitated Heptane Droplets. Photonics. 2024;11(11). doi:10.3390/photonics11111044. My contribution to this was to perform the experiments and write the manuscript.

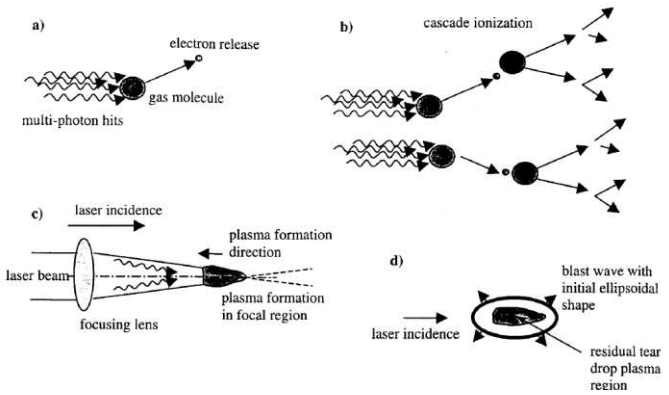

Figure 2.1: Schematic of the different stages for laser induced breakdown using nanosecond pulses. (a) Multiphoton ionization, (b) electron avalanche ionization, (c) plasma growth, (d) blast wave propagation[62]

mixture. However, for successful formation of laser spark MPI is not sufficient. Plasma formation and growth occurs only when there is a rapid generation of free electrons to counteract the various loss mechanisms such as electron diffusion, attachment, or recombination. This is achieved through the process of electron avalanche ionization[36,61] or cascade ionization shown schematically in Figure 2.1b. The seed electrons generated through MPI rapidly gain energy through inverse Bremsstrahlung absorption of laser radiation and upon further collision with surrounding molecules, induce further ionization of the gas molecule. This process leads to rapid multiplication of free electrons. The EAI reaction can be described as follows:

$$e^- + h\nu + M \rightarrow 2e^- + M^+ \tag{2.2}$$

The competing roles of MPI and EAI vary with conditions including wavelength, pulse duration and gas conditions [63,64]. Most of the plasma heating occurs during this phase of plasma formation. In the subsequent stages of plasma formation, plasma is observed to propagate along the beam path growing towards the laser source as shown in Figure 2.1c. The final stage involves the

formation of a blast wave (shown in Figure 2.1d) that propagates outward from the main plasma kernel.

2.2 Laser Induced Breakdown Spectroscopy (LIBS)

Laser Induced breakdown spectroscopy (LIBS)[65] is a widely employed diagnostic technique across various fields due to its ease of implementation and minimal equipment requirement. As illustrated in Figure 2.2, a LIBS system involves directing a pulsed laser beam onto the target medium, causing molecular dissociation and the formation of plasma through mechanisms like MPI and EAI, as detailed in the preceding section. Following plasma cooling and a reduction in ionization levels, the electronically excited atoms undergo relaxation, emitting element-specific radiation (atomic emission). This emitted radiation is scrutinized using a spectrometer coupled with an intensified charge-coupled device (ICCD) detector. Analysis of the identified spectral lines provides valuable information on the existence, concentration, and mass of species. LIBS showcases versatility by facilitating the examination of gases, liquids, solids, and aerosol systems. In this research we employed LIBS as the primary diagnostic to detect atomic lines of interest in laser ignition of sprays and droplets.

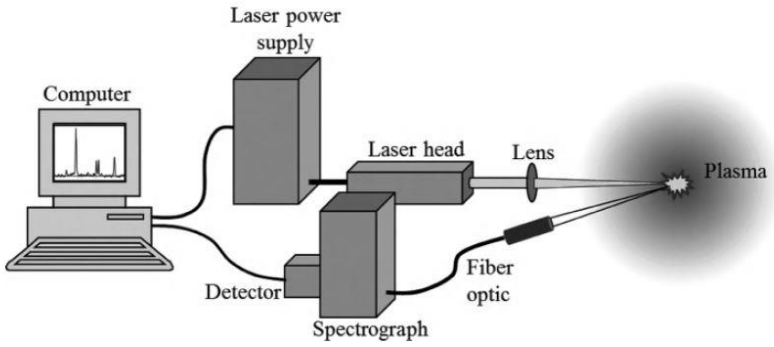

Figure 2.2 The diagnostic process and the necessary equipment for Laser-Induced Breakdown Spectroscopy (LIBS).[65]

2.3 Experimental Setup and Methodology for the Study of Laser–Droplet Interactions

2.3.1 Optical setup

Figure 2.3a illustrates the experimental setup employed in this investigation[66] for the study of laser-droplet interaction. For the laser ignition source, an Nd: YAG laser (Continuum custom system) with a 35 ns pulse duration, operating at a repetition rate of 5 Hz and emitting light at a wavelength of 1064 nm was utilized. To control the laser energy, a variable attenuator, formed from a half-waveplate and polarizer was used, to set the laser energy with values given below (shot-to-shot energy variation of ~3%). A Galilean telescope (f = -100 mm and f = 200 mm) expanded the laser beam by 2x resulting in a collimated beam diameter of ~25 mm. The collimated beam is finally focused with a 100 mm plano-convex lens to achieve a beam waist of ~0.1 mm (based on burn paper measurement) at the droplet location (held within the levitator) with a Rayleigh range of ~5 mm.

To create a controlled environment for the study of laser breakdown on droplets, a single-axis acoustic levitator (TinyLev, Makerfabs) was utilized to suspend a single heptane droplet in ambient air (shown in Figure 2.3b). The levitator, as described in Marzo et al.[67] uses an array of 72 ultrasonic transducers operating at 40 kHz to generate a standing wave, with nodes used for trapping liquid and solid particles. However, this setup has limitations, particularly in trapping droplets below a diameter of ~500 μm, where the acoustic streaming force induces significant oscillations[68], leading to the droplet detaching and being laterally displaced from the trap region. Experiments were conducted with three different laser energies: 35 mJ, 80 mJ, and 100 mJ over a droplet diameter range of 0.7 – 1.7 mm.

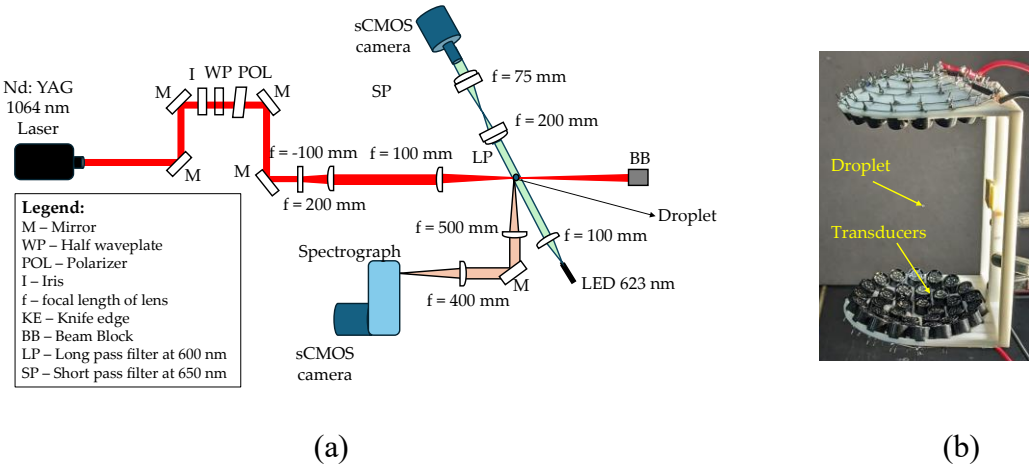

(a) (b)

Figure 2.3: (a) Experimental setup for laser irradiation of heptane droplet showing LIBS and shadowgraphy diagnostics; (b) Single-axis acoustic levitator used to suspend the droplet in air.

Multiple optical diagnostic techniques were employed to study the laser-droplet interaction and plasma formation[69]. For the spatial and temporal analysis of laser plasma optical emissions, LIBS was used, while shadowgraphy was used to capture images of droplet fragmentation resulting from the laser interaction. To enable spatial mapping of LIBS measurements, a periscope was used to adjust the collection height and rotate the image along the horizontal laser beam to align with the vertical input slit of the spectrometer. A combination of lenses was used to achieve a magnification of 0.8 (f = 500 mm and f = 400 mm) to collect the light and couple it to a spectrograph and camera. The spectrograph (Andor Kymera 328i) employed a 100 µm slit width and a grating with 300 grooves/mm, offering a theoretical resolution of 1.01 nm. The spectra were recorded using an sCMOS camera (Andor iStar) with an intensifier gain level of 4000, variable gate width providing a resolution of 7.7 µm/pixel. For shadowgraphy, light from a red LED (emitting light at 623 nm) was collimated by using a lens with a focal length of 100 mm and a telescope (f = 200 mm and f = 75 mm) was employed to magnify and focus the image onto an sCMOS camera (Andor iStar). The camera's resolution was 3.5 µm/pixel. The shadowgraphy is used primarily for direct imaging of droplet breakup dynamics but its images are also used to spatially reference the recorded LIBS

spectra (relative to the initial droplet position). Some regions in the shadowgraph images (shown in the subsequent sections) at specific time delays appear saturated. While the original image is unsaturated, we adjusted the brightness of the images to show various features like the blast waves and droplet fragments.

2.3.2 Spatial LIBS Methodology

Figure 2.4 shows the method employed to implement spatially resolved LIBS measurements (relative to the initial droplet location and surrounding gaseous regions). The overall approach was to spatially reference the 1-D spatially resolved LIBS spectra with 2-D images of the droplet at early time from the shadowgraphy. As an illustrative example, both the shadowgraph image (Fig. 2.4a) and the raw spectral image (Fig. 2.4c) were captured at the same time delay and gate width, which are 1000 ns and 100 ns respectively in this case. In Fig. 2.4b the pixel intensity versus distance along the laser beam direction is plotted from the 2-D shadowgraph image (using the magenta region in Fig. 2.4a). The images were divided into a series of spatial ribbons, each 50 pixels wide (~175 μm), along the laser beam direction. Then a threshold intensity value (determined from multiple datasets) was applied to differentiate between regions without a droplet (Intensity > 400 [a.u]) and then assume that remaining regions do contain a droplet. The regions close to the boundary between droplet and no droplet regions where the threshold algorithm misassigned the regions as such were rejected. Furthermore, based on the pixel location, the laser illumination side and the shadow (laser exit) side for the regions with no droplet were distinguished. The red dotted lines in Figure 2.4a indicate the shadow side of the droplet, the blue dotted lines represent the droplet region, and the green dotted lines denote the illumination side of the droplet. To find the corresponding location of the droplet on the spectrometer, a linear transfer function that maps the location of pixels from one camera to the other (based on viewing a grid on

both detectors) was developed. In Figure 2.4c, the red, blue, and green dotted regions represent the shadow side, droplet, and illumination side, respectively.

To generate the spectra from the spectrometer, a 50-pixel long ribbon along the detector (spatial direction) was averaged. Additionally, to account for the background (dark counts and stray scattering), another ribbon was selected from the bottom of the camera sensor (a region that did not receive any light), and averaged and subtracted from the main spectra. In Fig. 2..4d, the variation in spectra for droplet region, and the illuminated side (there was no detectable emission on the shadow side for this case) are shown. Note that the spectrometer is also calibrated for (relative) intensity using an LS-1-CAL tungsten-halogen light source.

2.3.3 Electron Density Determination by Stark Broadening

The electron density (n_e) was determined by analyzing the Stark broadening of H_α emission line at 656 nm. Traditionally, electron density estimation relied on the Stark broadening of Hydrogen Balmer lines, which show significant broadening due to the linear Stark effect. The Gigosos-Cardenoso model (GC)[70,71] was used to calculate electron density as this model also considers collisional/Van der Waals broadening and instrumental broadening. Natural, Resonance, and Doppler broadening (at temperatures as high as 10,000 K), were neglected as each contributed to less than 5 pm[72]. The H_α FWHM due to Stark broadening $\Delta\lambda_{Stark}$ (nm)[71,72] is determined as:

$$\Delta\lambda_{\text{Stark}} = 8.33 \text{ x } 10^{-3} \left(\frac{n_e}{10^{20}}\right)^{\frac{2}{3}} \tag{2.3}$$

where n_e is the electron density (m^{-3}).

The FWHM for Van der Waals broadening, $\Delta\lambda_{\text{vd } Waals}$,of H_α is calculated (in nm) as[71,72]:

$$\Delta\lambda_{\text{vd } Waals} = 0.1 \text{ x } \frac{p}{\left(\frac{T_g}{300}\right)^{0.7}} \quad (2.4)$$

where p is the pressure (bar) and T_g is the gas temperature (K). The instrumental broadening of the spectrometer was measured with a He:Ne laser at 543 nm by fitting a Lorentzian function as 0.48 nm (in rough agreement with calculation based on grating and monochromator parameters). In Figure 2.5, method used to fit the H_α line using a Lorentzian profile in Matlab with an open source peakfit [73] code is shown. Furthermore, the electron density was obtained based on assuming that the resulting lineshape is Lorentzian broadened with contributions from only Stark, Van Der Waals, and instrumental broadening as follows:[35]

$$\Delta\lambda_{\text{Stark}} = \Delta\lambda_{measured} - \Delta\lambda_{\text{vd } Waals} - \Delta\lambda_{instrumental} \quad (2.5)$$

where the uncertainty in electron density measurements was estimated based on the method discussed in Van der Horst et al.[72] and found as ~±25% with the fitting error contributing the most.

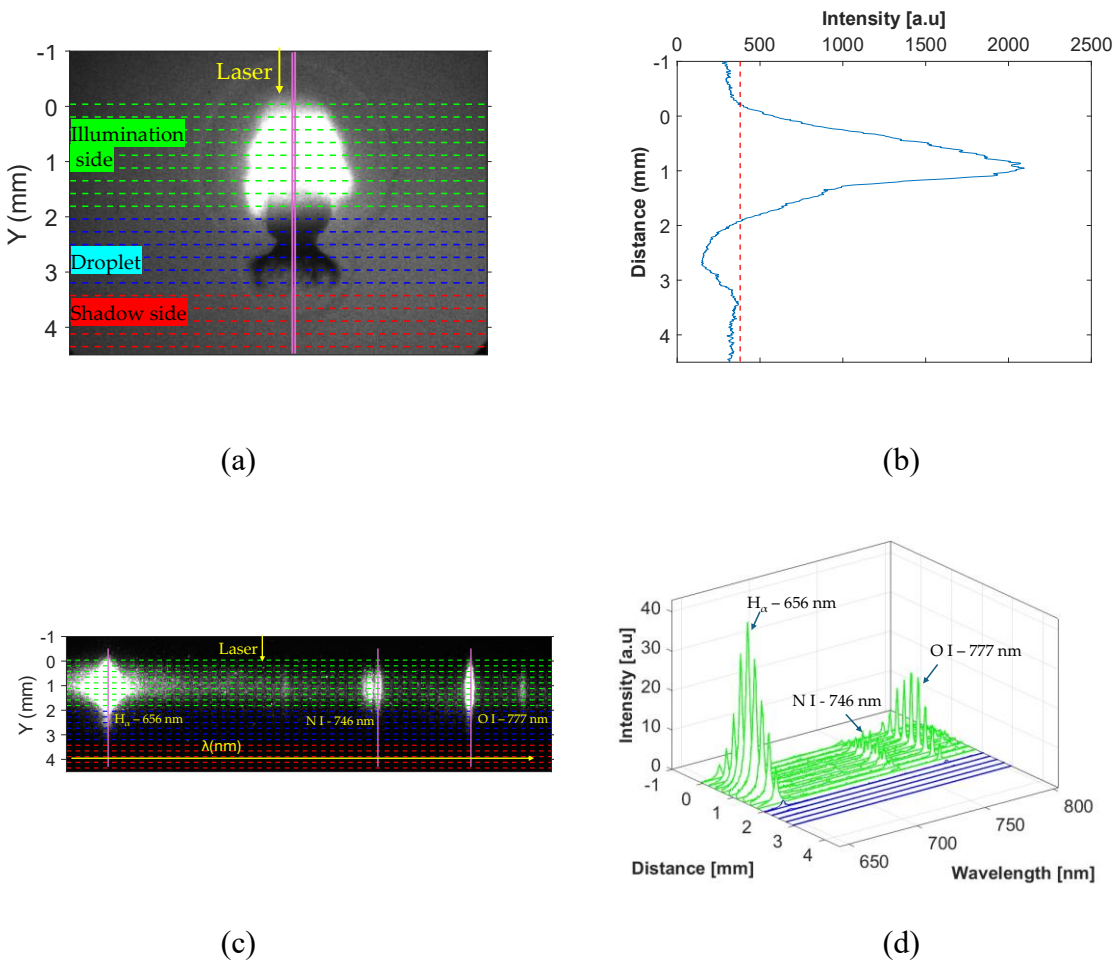

Figure 2.4: Spatial LIBS procedure (a) 2-D shadowgraphy image, (b) Intensity from 2-D image (found from magenta region in 2a) plotted against axial distance along laser direction, (c) Raw spectral image showing spectral data versus spatial position (along laser), (d) Representative spectra in the illumination side and droplet region. The spectra in the shadow side (red region) is not shown due to absence of emission. Laser energy – 80 mJ, Droplet diameter – 1 mm, Camera delay – 1 μs, Gate Duration – 100 ns.

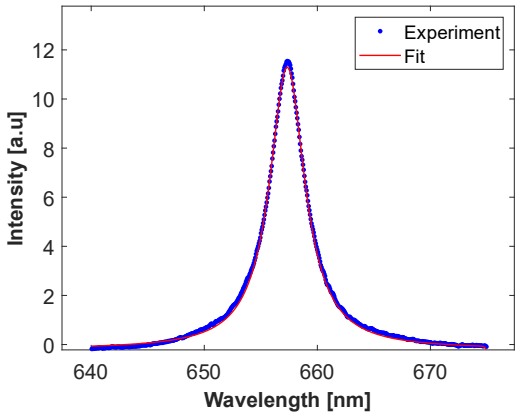

Figure 2.5: Curve fitting of H_α line emission from heptane droplet irradiation with laser. Laser energy – 80 mJ, Droplet diameter – 1 mm, Camera delay – 1 μs, Gate Duration – 100 ns.

In addition to determining the electron density, optical emission spectra of O lines was utilized to measure the plasma gas temperature. Assuming the plasma is in Local Thermodynamic Equilibrium (LTE), the Boltzmann plot method was employed to estimate the plasma temperature using the atomic oxygen lines at 715 nm and 777 nm. These lines were chosen based on their strengths and upper-level energy spacing. The plasma temperature is found as[53]:

$$kT = \frac{E' - E}{\ln\left(\frac{Ig'A'\nu'}{I'gA\nu}\right)} \tag{2.6}$$

where I is the total emitted line intensity (wavelength-integrated), ν is the line center frequency, g is the statistical weight, E is the transition upper-level energy, and A is the Einstein coefficient for spontaneous emission (for two lines ‘ and unprimed). While deviations from LTE can occur, the high electron densities, electron temperatures and short time scales associated with laser-induced breakdown plasmas typically support the LTE assumption, especially in the core region of the plasma[53,74]

In Figure 2.6, curve fitting of both the O lines with a Voigt profile using the peakfit[73] code to calculate the total intensities is illustrated. The uncertainty is estimated based on the method given in El-Rabii et al.[53] and is about 30% with the uncertainty in Einstein coefficients and measured areas contributing the most.

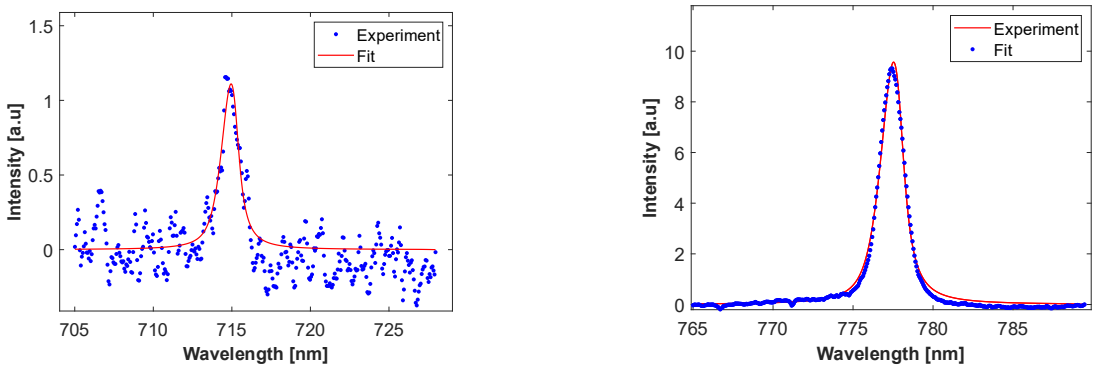

(a) (b)

Figure 2.6: Curve fitting of O line at 715 nm (left) and O triplet at 777 nm (right) emission from heptane droplet irradiation with Laser energy – 80 mJ, Droplet diameter – 1 mm, Camera delay – 1 µs, Gate Duration – 100 ns.

2.4 Experimental Setup and Methodology for Spray Ignition Study

Figure 2.7 illustrates the experimental setup used for spray ignition study. A vertically mounted annular co-flow spray burner (ACS) was used for spray ignition. The burner and nozzle were characterized in previous works[75] for various fuels, including n-heptane. The airflow rate was regulated using a mass flow controller (Alicat MFC, model?) with high accuracy (±0.8% of reading and ±0.2% of full-scale), while the fuel flow rate was controlled by a high-pressure syringe pump (ISCO, Model 260D). The ACS burner was placed on a three-axis kinematic stage to change the relative spark position in all three directions. All the experiments in this study were conducted at fixed air fuel flow rate of 250 SLPM and fuel flow rate of 50 ml/min. A Nd: YAG laser (Continuum

custom system) with a 35 ns pulse duration, repetition rate of 5 Hz, and a wavelength of 1064 nm was used for laser ignition. A variable attenuator, formed from a half-waveplate and polarizer combination was used to control the laser energy without affecting the beam profile or temporal characteristics. The shot-to-shot variation of laser energy was ~3%. A Galilean telescope with focal lengths of −100 mm and 200 mm expanded the laser beam by a factor of 2, resulting in a collimated beam diameter of ~25 mm. The collimated beam was then focused with a 250 mm plano-convex lens to achieve a beam waist of ~0.2 mm (based on burn paper estimate) with a Rayleigh range of ~5 mm. The laser was focused at 40 mm above the burner in all the test cases.

Several optical diagnostic techniques were used to investigate the ignition kernel evolution and its interaction with the spray. LIBS was employed to collect optical emissions of combustion relevant radicals including H, O, N, OH, CH, CN, and C_2. A combination of lenses were used to achieve a magnification of 0.7 (f = 500 mm and f = 350 mm) to collect the light and couple it to a spectrograph and camera. The spectrograph (Andor Kymera 328i, Belfast, Northern Ireland) employed a 100 μm slit width and a grating with 300 grooves/mm, offering a theoretical wavelength resolution of 1.0 nm. The spectra were recorded using an sCMOS camera (Andor iStar, Belfast, Northern Ireland) with an intensifier gain level of 4000 and variable gate width and delay, providing a spatial resolution of 7.7 μm/pixel.

The acquired spectra were analyzed using MATLAB with the open-source peakfit[73] code. A Lorentzian function was employed to fit the Stark-broadened H line at 656 nm, while a Voigt function was used to fit the O I triplet at 777 nm. The integrated areas (and associated fitting errors) of the H and O lines were used to compute the H/O spectral ratios, including the corresponding uncertainty. Although a relative spectral response calibration was not performed, this omission does not affect the interpretation of trends or relative changes in the H/O area ratios. Additionally,

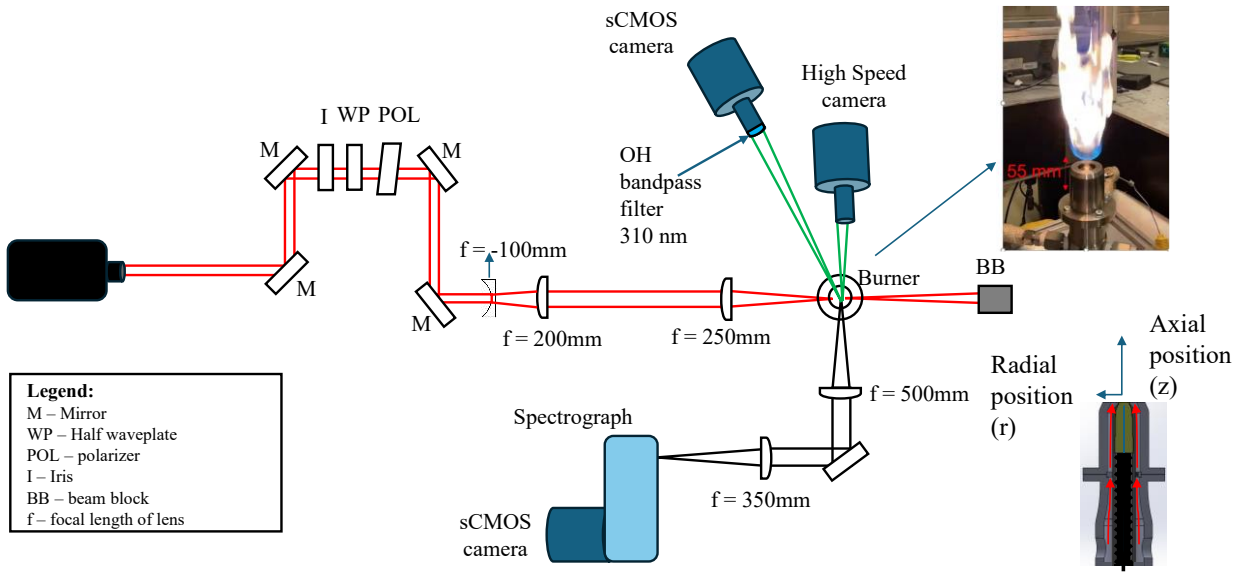

Fig. 2.7: Experimental setup for laser ignition and diagnostics of spray. Inset at top right shows a photograph of the burner flame operating on an n-heptane flame (Fuel – 40 ml/min, Air – 200 SLPM). Inset at bottom right shows the coordinate convention for ignition locations.

the CH band emission ($A^2\Delta \rightarrow X^2\Pi$ (0–0), with a peak near 432 nm was analyzed to differentiate between ignition and failure modes. This spectral band was also fitted using a Voigt function to quantify the CH intensity. A statistical analysis of the number and size of ignition kernels was also conducted using an intensified camera (Andor iStar sCMOS). Figure 2.8a shows an image of the corresponding plasma kernels captured with 50 ns gate-width centered on the laser pulse. The corresponding intensity profile, shown in Figure 2.8b, illustrates the method used to identify and characterize individual kernels. Peaks in the intensity profile were used to count the number of kernels, while the kernel size was estimated from the spatial full-width-at-half-maximum (FWHM) of each peak. The total kernel length was obtained by summing the individual kernel widths.

OH chemiluminescence imaging was also used to characterize the ignition modes in this study by using an intensified camera (Andor iStar sCMOS) with a bandpass filter (Andover) with a center wavelength of 310 nm. The camera was operated with a gain of 4000 and the images were captured at varying delays from the laser pulse with variable gate widths, providing a resolution of 27

μm/pixel. Finally, high-speed imaging was employed to track the evolution of the flame from laser deposition to the formation of a self-sustained flame. A high-speed camera (Photron Fastcam SA5) operating at a 40 kHz frame rate was used to this end with an image resolution of 0.15 mm/pixel.

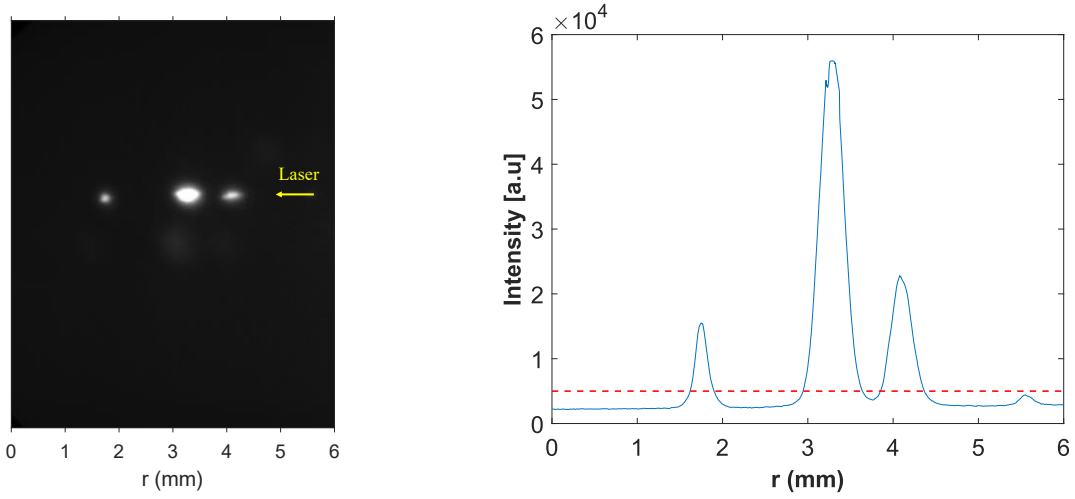

(a) (b)

Fig. 2.8 (a) Location of spark kernels Image captured on sCMOS (b) Intensity from spark kernel plotted against axial distance along laser direction.

Table 2.1 Summary of experimental conditions

	Laser Energy (mJ)	Radial ignition location (mm)
Set #1	125	20
		30
		40
Set #2	30	0
	50	0
	80	0
	80	10
	150	0
	250	0

Table 2.1 summarizes the experimental conditions for the two sets of tests performed. In both cases, the air flow rate was held constant at 250 SLPM, and the fuel flow rate was fixed at 50 mL/min. The first set of experiments focused on examining the effect of local fuel-air ratio and kernel characteristics on spray ignitability. The second set investigated how varying laser energies and ignition locations influence ignition outcomes and failure modes.

CHAPTER 3: Laser Induced Breakdown Spectroscopy and Shadowgraphy of Acoustically Levitated Heptane Droplet[2]

This chapter presents the results from the laser–droplet interaction study conducted using an acoustic levitator and the optical setup described in Chapter 2, Section 2.3. Both laser energy and droplet size were systematically varied to investigate different droplet fragmentation regimes. Droplet fragmentation dynamics were visualized using shadowgraphy, while Laser-Induced Breakdown Spectroscopy (LIBS) was employed to identify the species present in the breakdown region and to quantify electron density and temperature. To resolve the plasma characteristics across the interaction domain, spatially resolved LIBS measurements were performed by mapping the reference images acquired from the camera to the corresponding emission spectra. This approach enabled the determination of breakdown locations and the inference of localized plasma parameters throughout the droplet interaction region.

3.1 Results and Discussion

3.1.1 Shadowgraphy of laser-induced droplet fragmentation

The fragmentation of droplets induced by a laser pulse is influenced by factors such as laser pulse energy, duration, and focusing conditions as well as the intrinsic droplet characteristics such as size, composition, and density[15,29]. When the laser is focused within the droplet, part of its energy is scattered and reflected while the droplet absorbs (and potentially refocuses) the remainder. This absorbed energy partly initiates plasma formation, causing droplet expansion and fragmentation,

[2] This chapter is based primarily on material published as a journal article: Lokini P, Dumitrache C, Windom BC, Yalin AP. Laser-Induced Breakdown Spectroscopy and Shadowgraphy of Acoustically Levitated Heptane Droplets. Photonics. 2024;11(11). doi:10.3390/photonics11111044. My contribution to this was to perform the experiments and write the manuscript.

while the rest dissipates into a blast wave. In some cases, plasma formation events occur at multiple locations within or around the droplet[29]. Bulat et al.[19] proposed that the fundamental mechanism behind laser-induced droplet breakdown is the explosive evaporation of the droplet. As the laser penetrates the droplet's core, it heats the droplet intensely, exceeding the saturation vapor temperature at the given conditions and creates an internal vapor cavity, or cavitation bubble, within the droplet. Subsequent laser pulse absorption increases the pressure within this cavity, generating plasma and initiating a blast wave. This expanding blast wave leads to thermal ionization of the surrounding (cavitation) gas and droplet species along its path. The resultant free electrons cause further ionization, continuing the breakdown process and culminating in rapid vaporization. Consequently, the droplet undergoes destruction through jetting or explosion. While Bulat et al.[19] do not specify the droplet size and laser energy required for this type of breakdown, several studies[15,16,76] experimentally verified this mechanism of droplet breakdown in water droplets at diameters of 3-4 mm with small laser energies (~2 mJ).

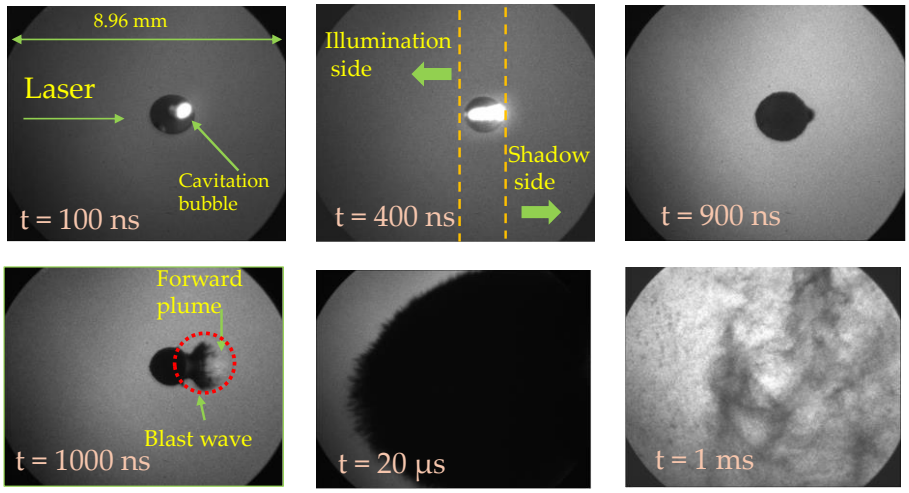

Figure 3.1: Time-sequence of shadowgraph images of laser irradiation of heptane droplet at laser energy of 80 mJ for droplet diameter of ~1.5 mm. The camera gate width is 100 ns.

Figure 3.1 illustrates the optical breakdown of a heptane droplet, approximately 1.5 mm in diameter, induced by a laser pulse at 80 mJ, captured at various time delays from the laser pulse. Although each image corresponds to a distinct experiment, the sequence is quite repeatable such that the panels illustrate the temporal evolution of droplet irradiation phenomena. At these laser and focusing conditions, optical breakdown in air (without the presence of the heptane droplet) was also observed. In the image shown at t = 100 ns (relative to the time of the laser illumination), strong luminous (plasma) region within the droplet, proximate to the droplet-air interface on the "shadow" (downstream laser) side was observed. This luminous region may be indicative of a cavitation bubble, likely consisting of heptane vapor, and suggests plasma breakdown primarily occurs at this location. At 400 ns, owing to rapid ionization and heating, the bubble/luminous region grows in size, engulfing the droplet. The plasma formation inside the droplet generates a blast wave (labeled forward plume) that propels the droplet fragments (as seen at 1000 ns) towards the shadow side of droplet implying non-uniform spatial energy deposition.

A time scale for cavitation formation and bubble growth can be determined from the Rayleigh-Plesset equation[77]:

$$t_{cav} = \frac{R_0}{\sqrt{P_{Laser}/\rho}} \tag{3.1}$$

where R_0 is the initial bubble radius (considered to be on the order of the beam waist) and ρ is the heptane density. The pressure inside the bubble after laser energy deposition, P_{Laser} comes from the rapid conversion of the absorbed energy into heat, which causes localized vaporization and a vapor bubble to form. This pressure can be estimated from the energy density in the region affected

by the laser. A rough estimate of the pressure rise inside the bubble can be obtained by assuming that the energy density is approximately equal to the work done by the expanding bubble:

$$P_{Laser} = \frac{E_{Laser}}{3V_{Laser}} \tag{3.2}$$

where the factor 1/3 is a consequence of averaging over the three spatial dimensions for energy distribution into the bubble, E_{Laser} is the laser energy, V_{Laser} is the initial volume of the spark . The substitution of laser parameters yields a characteristic time scale for the bubble development is ~30 ns (prior to explosion) which agrees with our empirical observations presented in Figure 5.

Additionally, at later delays (10 µs and 1 ms), the droplet undergoes catastrophic fragmentation, disintegrating into smaller fragments. Overall, when the laser passes through the droplet, the front side (entrance) appears to undergo a relatively weaker disturbance, while the exit experiences intense energy buildup and eventual fragmentation. Hsieh et al.[78] noted this type of fragmentation in water droplets in an argon atmosphere with a 532 nm laser, and several other studies[15,16,29] also documented this in diesel[15] and biodiesel droplets48.

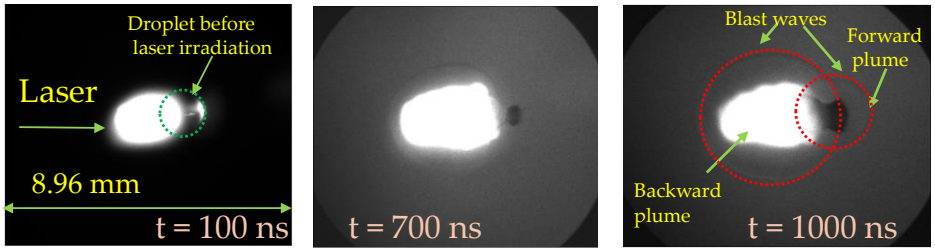

Figure 3.2: Time-sequence of shadowgraph images of laser irradiation of heptane droplet at laser energy of 80 mJ for droplet diameter ~1.0 mm. The camera gate width is 100 ns.

Figure 3.2 depicts a qualitatively different optical breakdown in this case due to a heptane droplet with a diameter of approximately 1 mm, induced by a laser pulse of 80 mJ, again captured at various time delays relative to the laser pulse. In comparison to the larger diameter (1.5 mm) case, at early time (100 ns panel), a prominent luminous (plasma) region was observed on the

illumination side (upstream side), as well as within the droplet, closer to the droplet-air interface on the shadow side. This may be indicative of two distinct breakdown events, contrasting with the single event observed in the case of the larger droplet. The plasma breakdown on the illuminated side appears to originate from the gas phase adjacent to the droplet, potentially incorporating the vapors from the droplet and may not have formed from the cavitation/vapor bubble route as described by Bulat et al.[19]. The second breakdown site, a weaker event occurring at the shadow side of the droplet, can be attributed to the droplet's ability to refocus[9] some of the laser energy. However, this results in a significantly weaker breakdown and blast, as much of the energy has already been expended in the initial breakdown. Furthermore, two blast waves generated from the two breakdowns, with a stronger blast wave on the illumination side and a weaker one on the shadow side of the droplet were observed. In addition to these blast waves, two jets, labeled as backward and forward plumes, are evident on both the illuminated and shadow sides of the droplet. These plumes show the expulsion of droplet fragments propelled outward from the droplet. Eickmans et al.[29] noted this type of fragmentation in water droplets with a 1064 nm laser at different intensities.

If the energy deposited by the laser pulse is large relative to the volume of the droplet, the droplet may not have time to undergo cavitation and instead it will disintegrate due to rapid phase transition or explosive boiling. This is supported by the experimental observation shown in Figure 3.1 and Figure 3.2. For a fixed laser energy of 80 mJ, quite different droplet fragmentation regimes based on the droplet size were observed. In the case of the 1.5 mm droplet, plasma emission was observed inside of the droplet and the droplet seems to maintain its structural integrity during the emission process for a relatively long time (~ 1 us) thus supporting the idea that cavitation has led to formation of plasma within the droplet. However, when the droplet size is reduced to 1 mm,

plasma emission is accompanied by droplet fragmentation almost instantaneously (images at 100 ns already show droplet fragmentation). It is posited that as the volumetric energy absorbed in the droplet increases, the droplet undergoes almost instantaneous disintegration without cavitation.

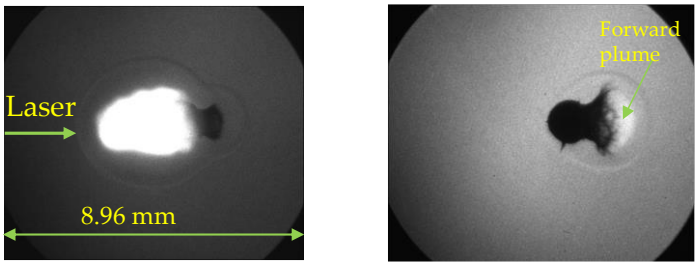

(a) (b)

Figure 3.3: Shadowgraph images of laser irradiation of 1 mm diameter heptane droplet at: (a) laser energy of 80 mJ (b) laser energy of 35 mJ. The camera delay is 1000 ns and gate width is 100 ns for all cases.

Figure 3.3a and 3.3b provide a comparison of droplet breakup dynamics for a droplet of 1 mm diameter but at two different laser energies of 80 mJ and 35 mJ respectively. Note that optical breakdown was not detected in air at 35 mJ. Despite the substantial difference in laser energy, the droplet fragmentation at 35 mJ closely resembles that observed at 80 mJ with a larger droplet diameter of 1.5 mm (Fig. 3.2). In both cases, a single blast wave originates from a single breakdown event occurring at the droplet-air interface on the shadow side, resulting in a forward plume.

The results so far indicate that the energy coupled into the droplet affect the breakup dynamics and energy distribution within the droplet. It is also worth noting that there may exist other fragmentation regimes beyond those examined in this study, that could result in different modes of optical breakdown within the droplet. Some research groups[19,20,29] have identified a lower energy regime where breakdown predominantly occurs near the shadow side of the droplet, with the remaining laser pulse sustaining breakdown growth that results in a blast wave. On the other

hand, a higher energy regime[29,78] is also observed, characterized by multiple breakdowns on both the illuminated and shadow sides of the droplet.

3.1.2 LIBS of laser-induced droplet fragmentation

Figure 3.4 shows single-shot LIBS spectra of air plasma over a range of 500-800 nm at various time delays relative to the laser pulse. The laser was focused using the same configuration as is employed for droplets with pulse energy of 80 mJ in this case. These data, collected in the absence of droplets, serve as a benchmark for the diagnostic system and will be crucial for subsequent comparisons with spectra acquired when droplets are present. At the earlier time delays, a high background contribution from bremsstrahlung emission (also known as free-free transitions) which decreases significantly with time[53] was noticed. The plot labels the atomic lines of N II at 648 nm and 661 nm, H_α at 656 nm, O I at 715 nm, 777 nm, and 794 nm, N I at 746 nm [79]. These lines are a result of the laser breakdown of ambient air, with N and O originating from the dissociation of molecular nitrogen and oxygen respectively, while H_α comes from the dissociation of naturally occurring water vapor in air[45]. These air plasma spectra are consistent with measurements from other researchers at similar conditions.[53]

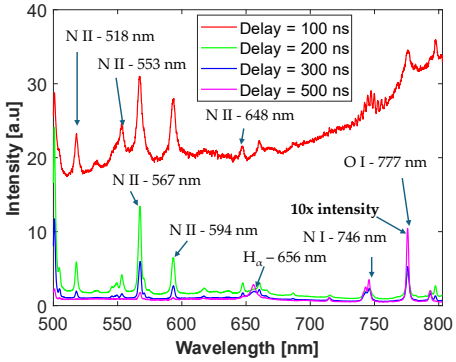

Figure 3.4: Emission spectra of air plasma at various time delays with atomic lines labeled. The spectrum at 500 ns is shown after multiplication by factor of 10 (for enhanced readability).

Figure 3.5a and 3.5b show the time-resolved LIBS spectra over the spectral range of 500-800 nm following laser irradiation of a heptane droplet with laser pulse energy of 80 mJ at diameters of ~1.5 mm and ~1 mm, respectively. The spectra are representative of all spatially integrated light from the droplets as found by averaging across all pixel (spatial) rows showing luminosity (the spatial variation in the spectra is discussed in the subsequent section). In the ~1.5 mm case (Fig. 3.5a) C_2 Swan bands at ~516 nm, ~563 nm, and ~600 nm are noted with no discernible atomic lines. The C_2 molecular bands are superimposed on a significant continuum emission that reduces with time. Eickmans et al.[29] also noted continuum emission from the laser breakdown of water droplets. The plasma inside the droplet is optically dense (electron density ~10^{18} cm^{-3}) such that the emission from the atomic species (internal to the droplet) is absorbed by the electrons. This radiation is then re-emitted by the electrons via Bremsstrahlung emission[80]. As discussed in the previous section, under these conditions only a single breakdown event and a single blast wave due to the reduced energy distributed among the heptane molecules was observed. This indicates that the energy is insufficient to dissociate the heptane into atoms, but it can lead to the formation of C_2 through the multi-photon dissociation[81] of heptane.

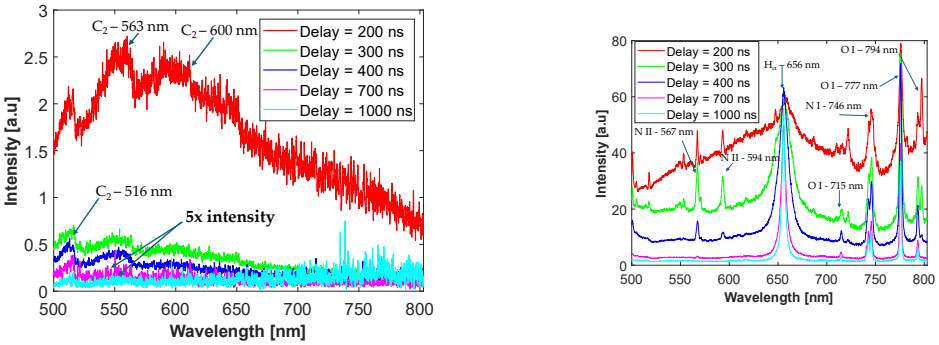

(a) (b)

Figure 3.5: Emission spectra of heptane droplet irradiated by laser at energy 80 mJ, at various time delays, for droplet diameter of (a) ~1.5 mm and (b) ~1 mm. The spectra in (a) at delays 700 ns and

1000 ns are shown after multiplication by factor of 5 for enhanced readability. Gate duration in all cases is 100 ns.

In the ~1 mm case (Fig. 3.5b) significant continuum emission superimposed on atomic lines of H_α, N, and O was noted at earlier delays compared to later times. The H_α (656 nm) emissions may be due to a combination of dissociation of the heptane (C_7H_{16}) molecule (liquid phase but also vaporized in air region adjacent to droplet) and partly from the dissociation of ambient water vapor. The atomic O and N lines originate from the dissociation (and excitation) of the oxygen and nitrogen molecules in the air surrounding the droplet.

These findings indicate that the breakup dynamics of the droplet are significantly influenced by the ratio of laser energy to the droplet's volume. Therefore, energy density metric, expressed volumetrically as energy per unit volume is proposed to classify the cases into the two observed regimes based on the experiments conducted at different laser energies (35mJ, 80mJ, 100mJ) and droplet diameters (0.7-1.7 mm). Figure 3.6 shows the impact of energy density on the type of breakdown or regime. Here regime 1 is defined as the scenario where only one breakdown (within the droplet) and its corresponding blast wave are observed, and regime 2 as the scenario with multiple breakdowns and blast waves. Furthermore, in terms of spectra regime 1 shows primarily C_2 bands but not atomic lines, while regime 1 shows atomic lines of H_α, O, and N. Regime 1 is present for energy density <~70 mJ/mm^3 while regime 2 occurs when energy density exceeds that value. A transitional regime is observed for energies densities in the range of ~60-80 mJ/mm^3 (which may also be due to experiments with slight misalignments between laser and droplet).

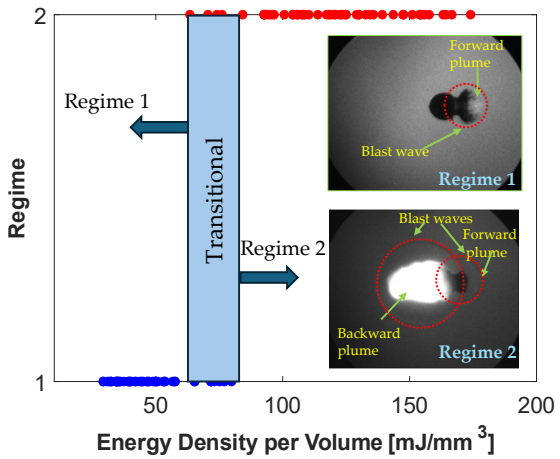

Figure 3.6: Mapping of energy density and regimes observed in the current study. Inset pictures are both captured at 1 μs from the laser with a gate duration of 100 ns and laser energy of 80 mJ and droplet diameter of ~1. 5 mm for Regime 1 and ~1 mm for Regime 2.

In addition to the reported regimes, other types of fragmentation are also noted in the literature[16,17,29,30] . Alternatively, the droplet mass could be used in place of droplet volume to develop this metric. Building on this approach, a dimensionless number could be formulated to account for factors such as droplet density, specific heat/latent heat of vaporization (to account for varying droplet compositions), initial droplet temperature, and ambient pressure, providing a predictive tool for determining the fragmentation regime.

3.1.3 Plasma parameters of heptane droplet

The obtained droplet spectra can be analyzed to infer electron density and temperature. As a means to validate our methods, a study for laser plasmas formed in air (no droplet present) was first performed. Figure 3.7a and 3.7b present the electron density and temperature measurements of the air plasma at laser energy of 80 mJ at various time delays compared to two related literature studies[53,82]. Since El-Rabii et al.[53] conducted their study with a 355 nm laser (34 mJ), and Boguszko et al.[82] conducted their study with a 532 nm laser (180 mJ), exact match to their values was not expected, however, observed values show similar magnitudes and trends. A reduction in

electron density with time was observed in all studies owing primarily to plasma recombination[59]. The temperature decreases with time because of rapid expansion and cooling of the plasma after plasma initiation including radiative losses and collisional processes[59].

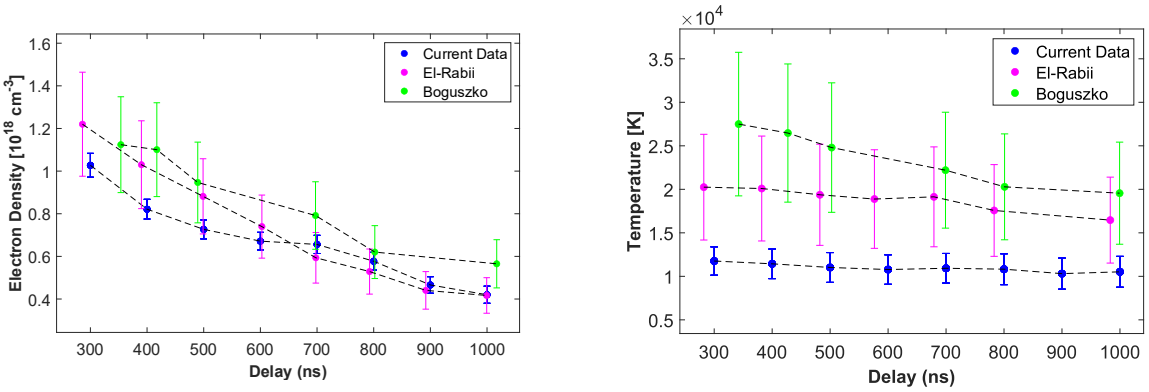

(a) (b)

Figure 3.7: Variation in (a) electron density and (b) gas temperature of air plasma with time delays from the laser pulse in air (no droplet) compared with literature[53,82]. Laser energy is 80 mJ.

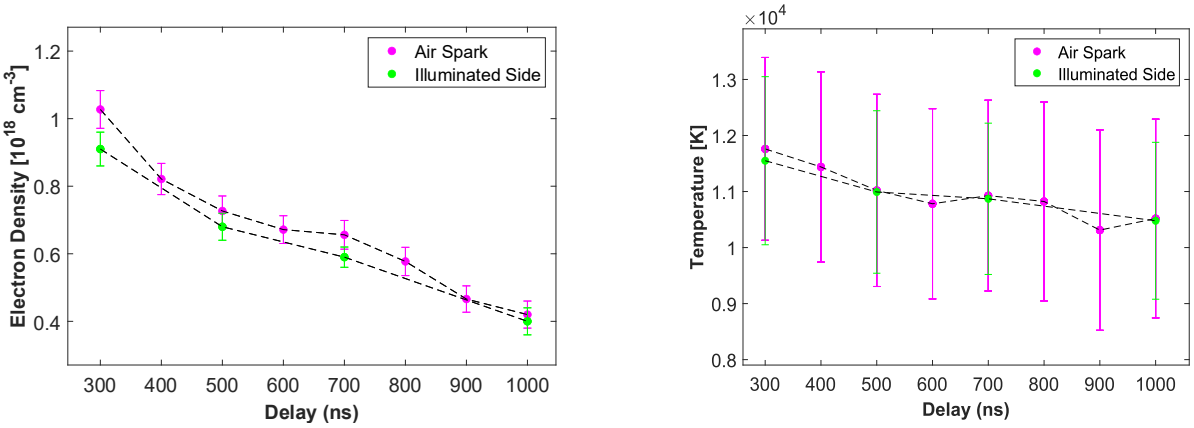

(a) (b)

Figure 3.8: Variation in (a) electron density and (b) temperature of heptane droplets with time delays from the laser pulse at laser energy 80 mJ and droplet diameter of ~1 mm (regime 2). The signal-to-noise ratio of O I at 715 nm and H_α at 656 nm was too low to estimate temperature and electron density in the droplet region, respectively.

Figure 3.8a and 3.8b depict the spatially resolved electron density and gas temperature measurements in heptane droplets of diameter ~1 mm (regime 2) at various time delays for the illumination side. The data are for laser energy of 80 mJ and compared with results from the air spark. A similar analysis is not possible for the regime 1 scenario due to the absence of spectral lines and the droplet region in regime 2 owing to low signal-to-noise ratio of the H_α at 656 nm. The electron density in the air plasma and on the illuminated side of the droplet are comparable, with the exception of early times. Similarly, the temperature of the air plasma closely matches that of the illuminated side of the droplet. Despite differences in species composition between air and heptane, the plasma parameters, including electron density and temperature, remain remarkably similar. This could be possibly because the ionization energies of heptane [83] (~10eV), nitrogen [84] (~15 eV) and oxygen[85] (~12 eV) in air are on the same order of magnitude. As a result, the laser energy needed to generate free electrons and heat them to high temperatures is comparable in both media, resulting in similar electron densities and temperatures.

3.1.4 Spatial LIBS of heptane droplet

Figure 3.9a and 3.9b shows representative spatially resolved spectra at laser energy of 80 mJ and at droplet diameters of ~1.5 mm and ~1 mm respectively. Using the spatial referencing scheme discussed in Section 2.2, spectra corresponding to the droplet region and illumination (upstream) side were obtained. Even though a blast wave is seen propagating from the shadow side of the droplet in both the regimes, emission lines or continuum in this region were absent. In ~1.5 mm scenario, C_2 bands at 516 nm and 563 nm in the droplet region were observed while the illumination side is devoid of any atomic or molecular bands. However, in ~1mm scenario, atomic lines of H_α and N in both illumination and droplet regions were noted. This supports our earlier

hypothesis about there being a single breakdown in ~1.5 mm (regime 1) and two breakdowns in ~1mm (regime 2).

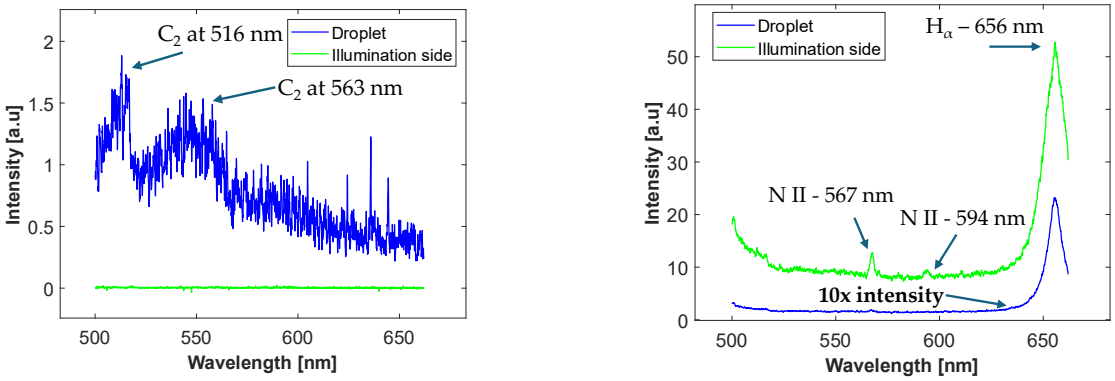

(a) (b)

Figure 3.9: Spatially resolved LIBS spectra due to droplet and illumination-side regions at laser energy 80 mJ for droplet diameters of (a) ~1.5 mm and (b) ~1 mm. The spectrum for droplet region in (b) is shown after multiplication by factor of 10 (for enhanced readability). All spectra use a time delay of 300 ns and gate width of– 100 ns.

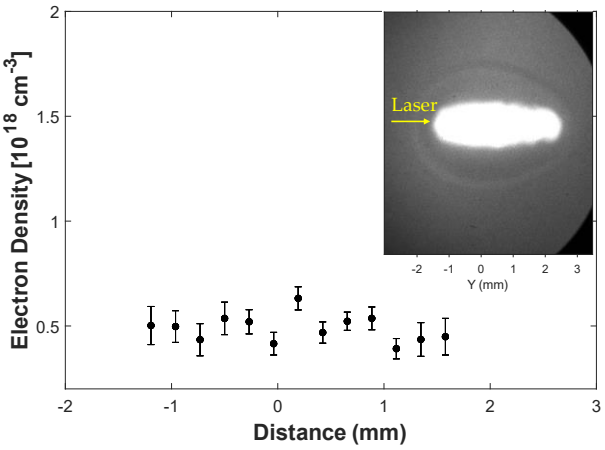

Figure 3.10: Variation of electron density over the length of air plasma at Laser energy – 80 mJ, Camera delay – 1 μs and gate duration – 100 ns. Inset shows the shadowgraphy image of the air plasma.

Figure 3.10 shows the spatial variation in electron density for an air plasma formed from focusing a laser at 80 mJ at 1 μs from the laser. The shadowgraphy image shown in the inset highlights the characteristic tear drop shape of an air plasma with broader waist oriented in the laser direction.

While the electron density variation in Figure 3.10 is based on a single-shot measurement, it is representative of similar spectra observed at this time interval in other instances as well. The electron density remains consistent over the length of the plasma since air is relatively homogeneous. Additionally, the constant electron density may also imply that laser energy is distributed uniformly along the plasma. The signal-to-noise ratio for the O 715 line was so low that spatially resolved temperature measurements for air plasma and droplet breakdown[45] were not possible.

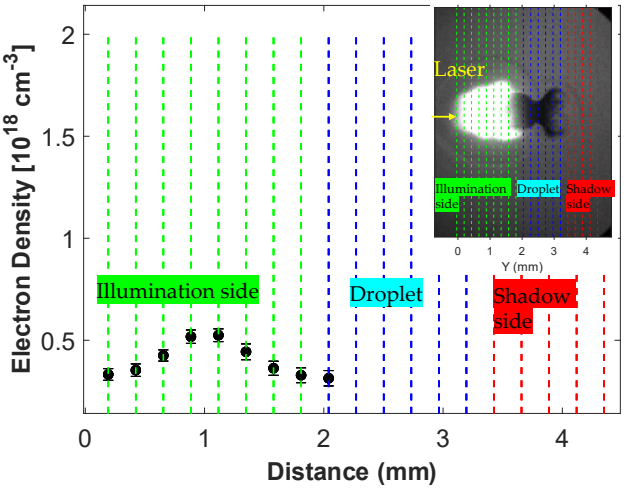

Figure 3.11: Variation of electron density over the length of heptane droplet breakdown at Laser energy – 80 mJ, Droplet diameter - 1 mm, Camera delay – 1 µs and Gate duration – 100 ns. Inset shows the shadowgraphy image with different regions of the breakdown labeled.

Figure 3.11 shows the spatial variation in electron density in the event of a breakdown of a 1 mm heptane droplet at laser energy of 80 mJ, 1 µs after the laser deposition. The shadowgraphy image shown in the inset shows the different regions in the droplet breakdown. Electron density was detected only in the illumination side. Unlike air plasma, in the droplet case, spatial variation in electron density was noted. The electron density is higher in the center of the illumination side and tapers off on both sides. While the air is relatively homogeneous, when the laser hits a droplet there are abrupt morphological changes . The laser pulse interaction with the denser liquid (droplet)

regions create more localized energy deposition which can rapidly vaporize and ionize the droplet and lead to a spatial variation in the electron density over the length of the plasma.

CHAPTER 4: Influence of Laser Energy and Ignition Location on Evolution of a Hydrocarbon Spray Flame[3]

This chapter presents the results of the laser ignition experiments conducted on a heptane spray. The 1st set of experiments were designed to investigate the effect of ignition location within the Laser-Induced Breakdown Spectroscopy (LIBS) was utilized to measure the H/O atomic intensity ratio as a qualitative indicator of the local equivalence ratio. In addition, the number and size of flame kernels were quantified to assess the relationship between kernel statistics and ignition success. In the second set of experiments both the laser pulse energy and ignition location were varied, and three distinct ignition outcomes were identified: short-mode failure, long-mode failure, and successful ignition. These modes were distinguished based on the flame kernel's extinction timescales, as captured through high-speed imaging. LIBS was further employed to detect emissions from combustion-relevant radicals such as OH and CH, providing additional insight into local chemistry. High-speed imaging not only visualized the evolution of flame kernels but also enabled quantification of kernel trajectories, offering a detailed view of kernel dynamics under different ignition conditions.

4.1 Results and Discussion

4.1.1 Representative LIBS spectra

Figure 4.1 shows single-shot LIBS spectra from an air plasma (control case) and a heptane-air mixture in the 640–790 nm range at a delay of 1 μs to the plasma deposition. Key atomic emission

[3] This chapter is primarily based on AIAA conference proceedings paper: Lokini P, Dumitrache C, Windom BC, Yalin AP. Simultaneous Laser Ignition and Laser-Induced Breakdown Spectroscopy of a Hydrocarbon Spray Flame. In: AIAA AVIATION 2023 Forum. AIAA AVIATION Forum. American Institute of Aeronautics and Astronautics; 2023. doi:doi:10.2514/6.2023-3603. My contribution to this was to perform the experiments and write the manuscript.

lines are labeled, including H_α at 656.3 nm (H_α and H are used interchangeably in this paper), N I at 746 nm, and O I at 777 nm. While H_α emission occurs primarily from the dissociation of water vapor in air, O I and N I originate from the dissociation of oxygen and nitrogen in air respectively. Spectral line identification was performed using the NIST database [79]. The O I emission is significantly stronger than H_α due to the low water vapor content in air (typically less than 2%). In the heptane-air spectra, H emission arises mainly from the dissociation of heptane, while O I and N I originate from the ambient air. Compared to air plasma, the heptane/air mixture exhibits a significantly stronger H signal, as expected due to the higher hydrogen content in the fuel. In the subsequent analyses, the ratios of these spectral features will be examined relative to the ignition outcomes.

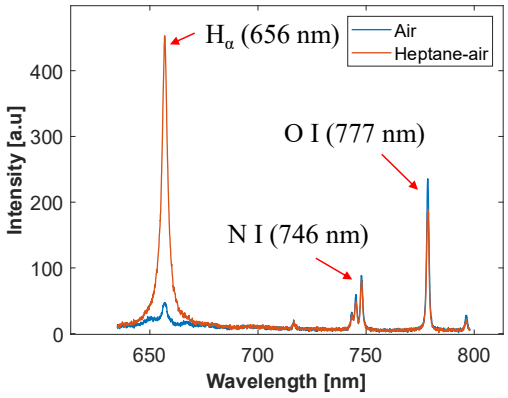

Fig. 4.1 LIBS emission spectra of air and heptane-air at a delay of 1 μs from the laser.

4.1.2 Ignition probability and average H/O from LIBS

Figure 4.2a shows the variation of ignition probability with radial ignition location at a fixed laser energy of 125 mJ and an axial ignition height of 40 mm (test conditions listed as Set #1 in Table 1).The following equation was used to calculate the uncertainty bars, based on standard deviation (σ), by assuming a normal approximation to the binomial distribution[41]:

$$\sigma = \pm Z\left(\frac{P(1-P)}{n}\right)^{1/2} \quad (1)$$

where P is ignition probability, n is the number of tests, and Z = 1.96 (based on 95% confidence).

Figure 4.2 b shows the average H/O ratio at the three radial ignition positions (with uncertainty bars due to standard deviation of repeats). These H/O ratios were obtained by averaging the total (wavelength-integrated) emission from the sparking events for ignition and no ignition cases due to H and O. A general decrease in the average H/O ratio was observed as the spark position moves farther from the burner, which is consistent with a lower concentration of the combustible mixture in those regions. Lee et al.[47] calibrated H/O ratios with local equivalence ratio and observed a similar decrease in equivalence ratio with increasing distance from the burner center. However, no significant difference in H/O was observed between ignition and no ignition events in the present study. While spectral ratios such as H/O may hold potential as indicators of ignition, these results suggest that additional spectral features or more comprehensive diagnostics would be necessary for reliable prediction.

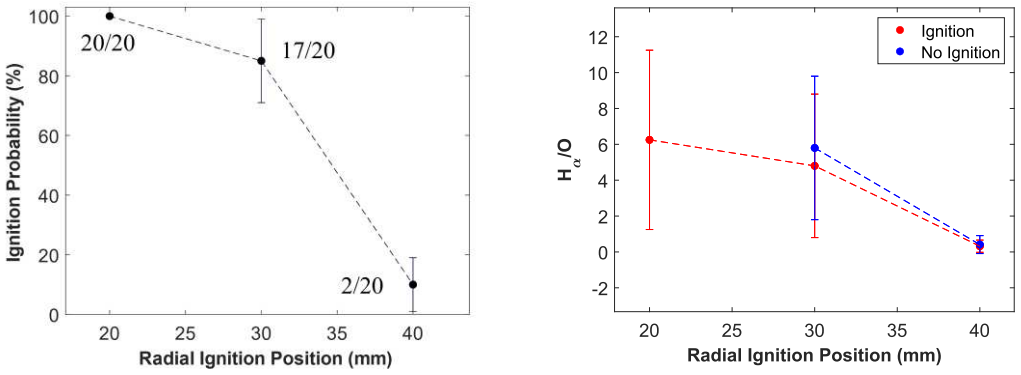

(a) **(b)**

Fig. 4.2 (a) Variation in ignition probability with radial ignition position (20 tests at each position with number of ignitions shown). (b) Variation of Hα/O for cases of ignition versus no ignition. All these tests were conducted at Laser energy = 125 mJ, z = 40 mm.

4.1.3 Early Flame Kernel statistics

Here, we consider statistical analyses of the early flame kernel(s), to look at possible correlation with extinction trends, using the methods of Section II. Figure 4.3a shows the variation in average number of kernels with the ignition position at laser energy of 125 mJ and axial ignition location of 40 mm (test conditions listed as Set #1 in Table 2.1). On average, more kernels are observed for spark locations closer to the burner centerline. This is likely due to higher droplet density near the centerline of the burner, which increases the probability of breakdowns since the breakdown threshold for droplets is lower than the gaseous fuel-air regions[33]. However, there is no significant difference in the average number of kernels between igniting versus non-igniting cases. Figure 4.3b presents the total kernel size, which remains relatively constant across different radial spark positions, but also does not show significant statistical differences between igniting and non-igniting cases. Figure 4.3c shows the variation in average kernel size with spark position. Interestingly, the average kernel size increases with distance from the burner center. This may be attributed to the distribution of laser energy. Near the centerline of the burner, energy is distributed over more droplets such that the energy deposition per droplet is likely lower thereby resulting in smaller kernel size, and vice versa far from the centerline. Again though, considering r = 30 mm, which is the only position with both ignition and non-ignition, we do not see clear size differences between those cases. Several studies[34,35] have also noted that in addition to kernel size, a number of other factors like the local flow dynamics and turbulence could also play a role in ignition of the spray. For example, Wawrzak and Tyliszczak[36] observed that interactions with vortical structures influence flame kernel development more significantly than the kernel size or number. Therefore, while both H_α/O ratios and kernel statistics provide useful insights into spray ignition behavior, they are not sufficient on their own to reliably predict ignition outcomes.

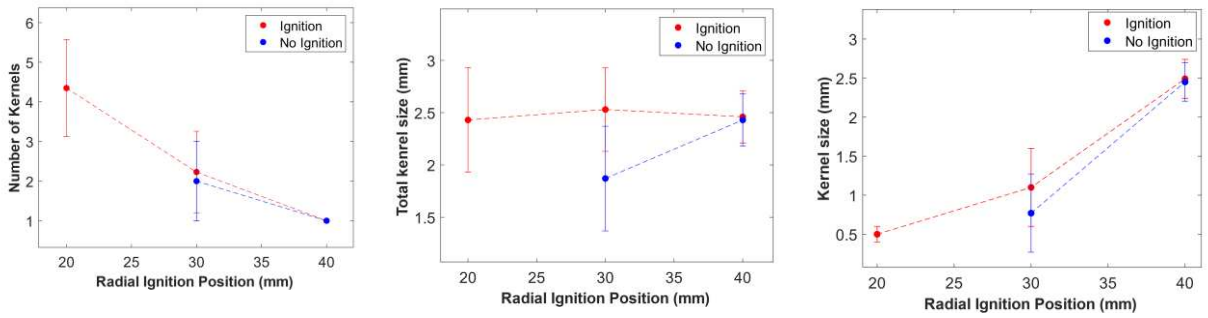

(a) (b) (c)

Fig. 4.3 Variation in (a) Number of kernels, (b) Total kernel size, (c) Kernel size with the radial ignition location for ignition and no ignition cases.

4.1.4 Classification of Ignition Failure and Success Events

In certain extinction test cases, a luminous ignition kernel that eventually extinguished was observed. This prompted further investigation using high-speed imaging to better understand the evolution of the flame kernel from the time of ignition to either a stable flame or extinction at test conditions designated as Set #2 in Table 2.1. Figure 4.4 presents representative high-speed image sequences of laser-ignited heptane spray at three laser energies—30 mJ, 80 mJ, and 250 mJ—with ignition initiated at the burner centerline, 40 mm above the burner surface, i.e., r = 0 and z = 40 mm. In ambient air, a visible spark was generated only at energies above 80 mJ. However, in the presence of the heptane spray, a spark was observed even at 30 mJ (Figure 4.4a, 0.1 ms) due to the reduced breakdown threshold caused by fuel droplets. At 30 mJ (Figure 4.4a), the kernel appears to drift away from the burner and extinguishes at time ~9 ms. At 80 mJ (Figure 4.4b), the kernel grows larger and propagates further before quenching at time ~31 ms. In contrast, 250 mJ (Figure 4.4c) results in a stable, self-sustained flame, indicating successful ignition. A kernel failure time was defined as the time of the last frame with an intensity above a predefined threshold.

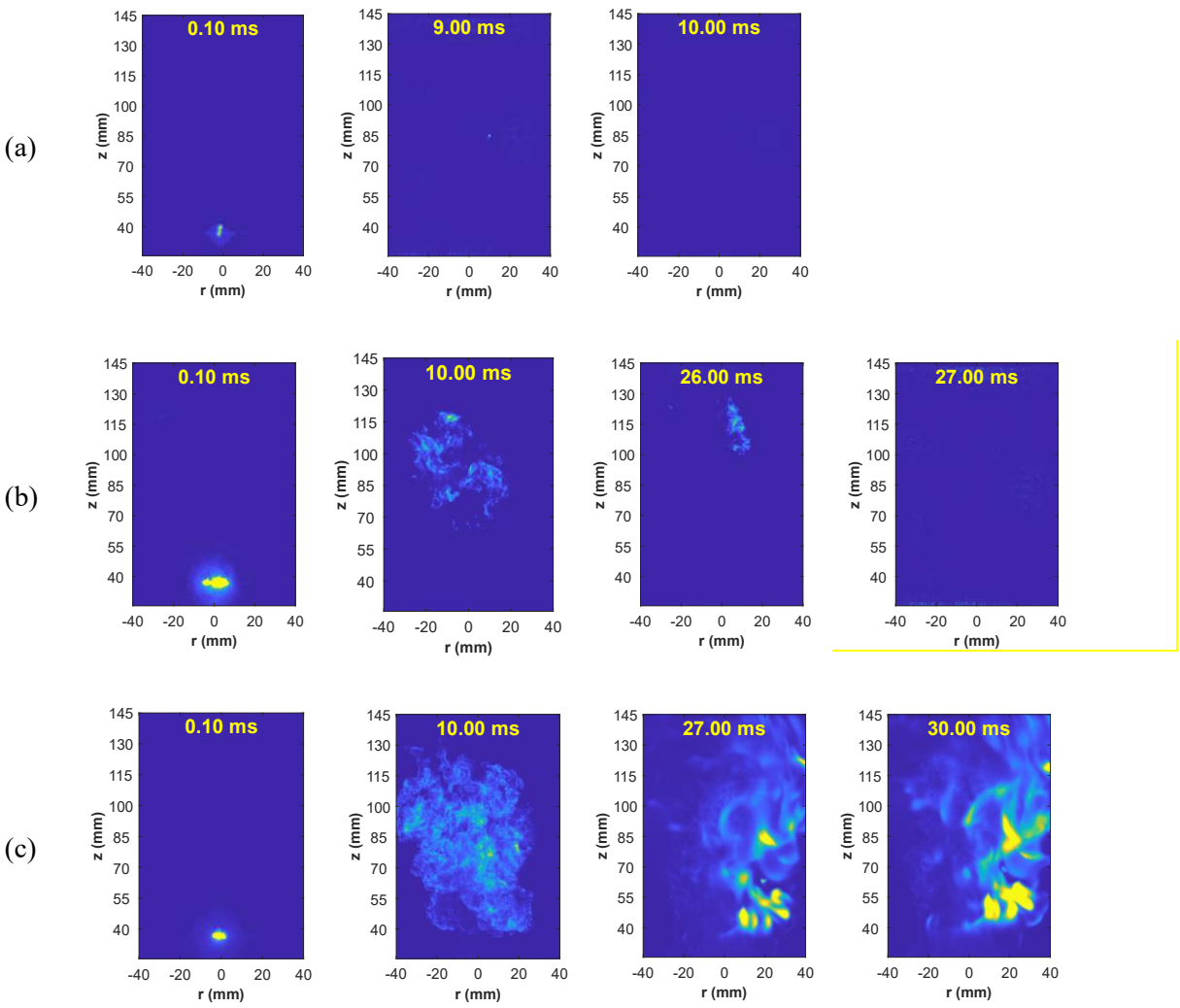

Fig. 4.4 High-speed images at different times for three events (a) Short-mode failure, Laser Energy = 30 mJ, (b) Long-mode failure - Laser Energy = 80 mJ, (c) Ignition - Laser Energy = 250 mJ. All tests were conducted at ignition location r = 0 mm, z = 40 mm.

The characteristic velocity for the burner used in this study was estimated based on the air flow rate of 250 SLPM, through an annular region with an outer diameter of 27.7 mm and an inner diameter of 10.7 mm[29]. This geometry yields an annular cross-sectional area (A) of ~ 512 mm². Based on the flow rate and the cross-sectional area, the volumetric flow rate ($\dot{V}$) is computed as ~ 4.167×10^6 mm³/s. From this flow rate and area, the characteristic velocity (U) was calculated to be ~8.14 m/s under standard conditions (1 atm, 298 K) using equation 4.1. The contribution of the fuel stream (50 ml/min of heptane) to the total volumetric flow was neglected in this velocity

estimate, as it constitutes less than 0.1% of the total volumetric flow rate.

$$U = \frac{\dot{V}}{A} \tag{4.1}$$

The flame kernel propagation height, determined from image processing (described in detail in section 4.1.7), was ~55 mm for ignition cases. Based on this height and characteristic velocity (U), the corresponding flow time scale is ~7 ms. Kernels extinguishing in less than 7 ms were therefore classified as "short-mode failures", while those persisting beyond 10 ms but still ultimately extinguishing were labeled as "long-mode failures". Finally, a test case was designated as a "successful ignition" when the flame stabilized, propagated self-sufficiently and then anchored itself. Figure 4.5 quantifies the kernel failure times and the probability of each mode across all tested laser energies. As can be seen, the selection of 10 ms as a separating threshold is appropriate to classify (delineate) the cases. Similar failure modes were reported by Oliveira et al.[3,13] for fuel–air sprays, although their time threshold for distinguishing short- and long-mode failures was significantly shorter (~0.5 ms) due to different experimental conditions (burner geometry, bulk flow velocities, and partial pre-vaporization of the fuel). Additionally, while multiple kernels were observed in this study, Oliveira et al.[3,13] usually noted single kernels, again, possibly because of the presence of prevaporized fuel resulting in a relatively homogeneous fuel-air mixture compared to the present study. The following sections further examine the physical mechanisms underlying the ignition failure modes.

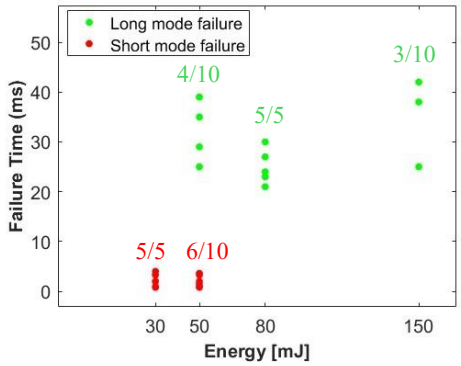

Fig. 4.5 Quantified flame kernel failure times at different laser energies, derived from high-speed image analysis.

4.1.5 OH chemiluminescence Imaging

Figure 4.6 shows representative OH chemiluminescence images captured 1 ms after laser deposition for the three ignition outcomes. Qualitatively, the OH signal (area and intensity) appears to be highest for successful ignition, followed by long-mode failure, and lowest for short-mode failure. Figure 4.7 presents corresponding OH images at 5 ms after laser deposition, where the distinction between ignition and long-mode failure becomes more pronounced. Based on the OH chemiluminescence images in Figures 4.6 and 4.7, the total area integrated intensity was computed and plotted in Figure 4.8a (at 1 ms) and Figure 4.8b (at 5 ms) for various laser energies. These values represent averages over multiple experimental runs. Data for 150 mJ at 1 ms were not acquired, and cases corresponding to 30 mJ and 50 mJ were excluded from Figure 10b since the flame kernels had generally extinguished by 5 ms. Across all tested energies, OH chemiluminescence consistently showed the highest intensity for successful ignition, decreasing through long-mode and short-mode failures. The increasing gap in OH between ignition and long-mode failure cases at 5 ms suggests that critical differences in flame development occur within the first few milliseconds following plasma.

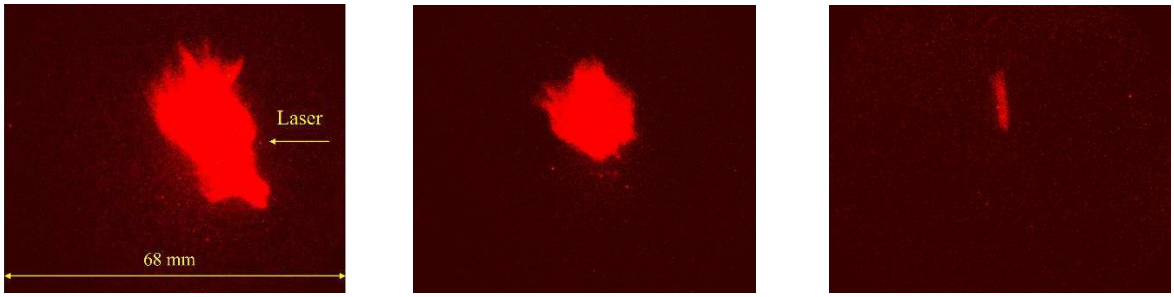

(a) (b) (c)

Fig. 4.6 Representative images of OH chemiluminescence acquired 1 ms after the laser deposition for (a) Ignition at Laser energy – 250 mJ, (b) Long mode failure at Laser Energy – 80mJ, and (c) Short mode failure at Laser Energy – 30 mJ. Camera gate – 1 ms. Scales in all panels are the same.

(a) (b)

Fig. 4.7 Representative images of OH chemiluminescence 5 ms after the laser deposition (a) Ignition at Laser energy – 250 mJ (b) Long mode failure at Laser Energy – 80mJ. Camera gate – 1 ms.

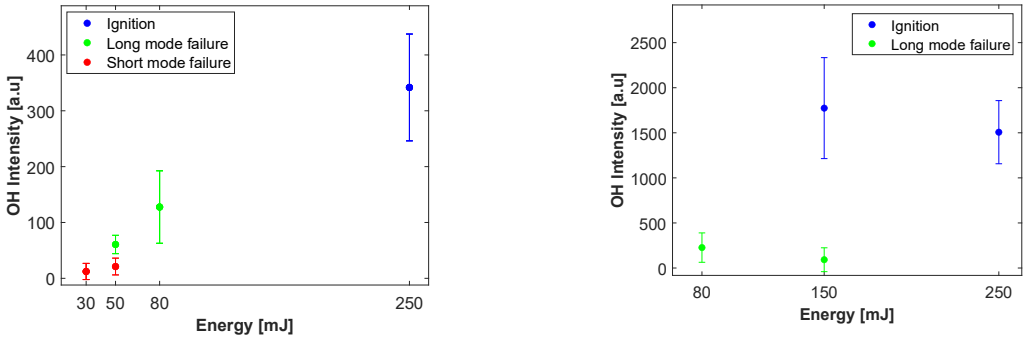

(a) (b)

Fig. 4.8 Variation of OH chemiluminescence intensity across laser energies and ignition modes. Data is based on OH images captured with camera gate – 5 ms and delays of (a) 1 ms, (b) 5 ms after laser pulse.

4.1.6 CH intensities from LIBS

Several groups have used atomic line ratios including H,O, and N [50,88–91] to quantify the local fuel-air ratio in gaseous fuel-air mixtures and correlate it with ignition. However, we did not observe a strong correlation between the H/O ratios (measured at 1 μs after laser spark deposition) and ignition. This suggests that, even at 1 μs, the dominant influence of the plasma may still obscure fuel-air ratio effects. To better capture the influence of fuel-air mixing on ignition kinetics, species measurements at later times may be necessary. However, atomic species undergo recombination at these timescales leading us to acquire molecular species signals at a delay of 100 μs.

Figure 4.9a illustrates representative emission spectra for ignition cases acquired 100 μs after laser plasma deposition. The species reveal the presence of key combustion species including OH, CH, CN, and C_2. In addition to OH, CH [5,47,92] is also a key marker of the flame front as it is a critical intermediate in the oxidation of the hydrocarbons. C_2 is formed during the decomposition of larger hydrocarbon molecules[47] and is an indicator of soot formation (precursor to polycyclic aromatic hydrocarbons (PAHs)). Figure 4.8b compares the CH intensities at different laser energies across multiple iterations. No spectra or signals were observed for laser energies below 80 mJ where short mode was observed. At 80 mJ only long-mode failures were detected, while at 250 mJ only successful ignition occurred. The CH intensities reflects this trend, with higher values corresponding to ignition cases and lower values to long-mode failures. At 150 mJ both long-mode and short-mode failures were observed. As previously mentioned, CH serves as an indicator of the flame front, and based on this data, it can clearly distinguish between successful ignition and long mode failure. While CH provides insights into why some cases ignite and others fail at 150 mJ, we hypothesize that additional factors, such as the influence of flow dynamics, may contribute to the variability in ignition outcomes.

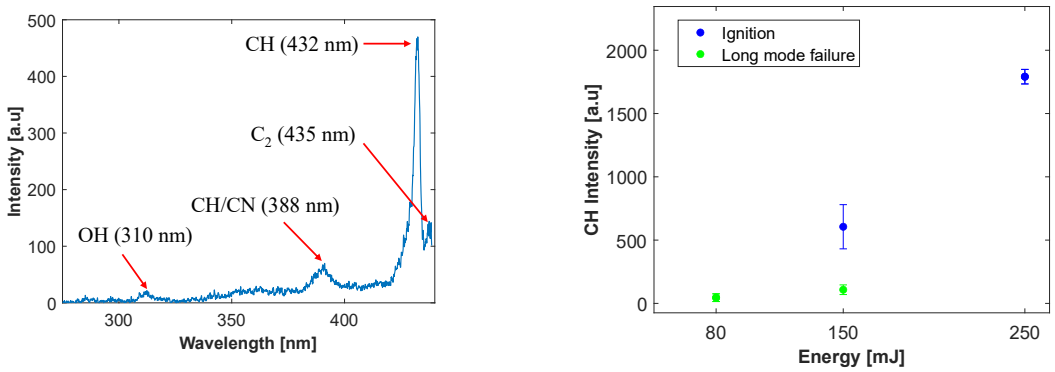

(a) (b)

Fig. 4.9 (a) Representative LIBS emission spectrum acquired for ignition cases at Laser – 250 mJ, (b) variation in CH intensity across different laser energies and ignition modes. Camera Delay- 100 µs, Gate – 5 ms.

Analysis of Figures 4.8 and 4.9b indicates that both OH and CH radical emissions provide valuable insights into the mechanisms underlying the identified failure modes. Short-mode failures exhibited low OH intensities, suggesting insufficient generation of reactive species and inadequate plasma kernel temperatures. This insufficient reactivity prevents the kernel from sustaining itself, resulting in rapid quenching within a few milliseconds. Such behavior aligns with prior observations by Marchione et al.[10], who identified a threshold in radical production below which ignition consistently fails due to insufficient chemical activity and heat release. In contrast, long-mode failures showed intermediate OH and CH emission intensities—higher than short-mode failures yet lower than successful ignition cases. The inability to transition from a surviving kernel to stable flame propagation in long-mode failures can be largely attributed to insufficient heat release to counteract cooling effects. Specifically, the energy provided by the laser at intermediate energies (e.g., around 80 mJ) is sufficient to initiate kernel formation and initial combustion activity but inadequate to sustain the vaporization and subsequent ignition of surrounding fuel droplets. The significant heat loss associated with evaporative cooling slows flame propagation and prevents the kernel from propagating upstream against the prevailing flow, causing eventual

kernel extinction[39,40]. Oliveira et al.[3,13] similarly observed a correlation between OH emission intensities and failure modes, further supporting the significance of radical species measurements as indicators of ignition success or failure.

The presence of both short-mode and long-mode failures at 50 mJ, and coexistence of long-mode failures and ignition at 150 mJ, highlights the inherent stochasticity in spray combustion processes. Such stochasticity in laser-induced ignition has been documented extensively in spray combustion literature, where slight fluctuations in local equivalence ratios[4], droplet clustering, and laser deposition characteristics[14,15] significantly influence ignition outcomes. Furthermore, flow dynamics such as turbulence intensity, local strain rates, and mixing efficiency significantly impact kernel survival and growth[36]. Turbulence can both enhance and impede flame kernel propagation by affecting heat and mass transfer processes. The subsequent section investigates the impact of flow-field characteristics on the ignitability of the spray.

4.1.7 Kernel Trajectories and Implications for Ignition

High-speed imaging was utilized to track flame kernel trajectories as a means to investigate the influence of local flow dynamics on spray ignitability. The kernel locations were identified using image processing in MATLAB. A threshold level of 0.08 (based on several data sets) was used to binarize the images. The kernel centroid was then computed as a weighted average of the centroids of individual subregions, with weights based on both pixel intensity and area. Figures 4.10a and 4.10b depict kernel trajectories over five independent trials at two different ignition locations at the same height above the burner of z = 40 mm both with the same laser energy of 80 mJ. Figure 4.10a is at r = 10 mm, where all the trails resulted in successful ignition and Figure 4.11b is at r = 0 mm where all the trails resulted in long-mode failures. The trajectories at r = 10 mm exhibited a characteristic downward trajectory following an initial upward motion which redirects heat and

reactive species toward the incoming fuel-air mixture, promoting sustained combustion. Such motion is consistent with the presence of a recirculation zone (near the burner), that facilitates enhanced mixing and longer residence times, thereby favoring ignition. In contrast, kernels generated at the centerline rose steadily upward, away from the burner, likely due to strong axial flow. This consistent upward motion inhibited interaction with the fresh mixture, contributing to flame kernel quenching.

Although the instantaneous flow field was not directly measured and is expected to be turbulent, symmetry-based considerations provide qualitative insight into the observed ignition behavior. At the burner centerline (r = 0 mm), the flow is dominated by upward momentum due to the axial injection of air and spray, resulting in predominantly upward streamlines. This is consistent with the observed kernel trajectories that rise away from the burner, limiting interaction with fresh reactants and leading to quenching. In contrast, at off-center locations (e.g., r = 10 mm), the flow is more likely to contain recirculation zones that could enhance ignition probability. Santiago et al. reported similar observations[41] in the burner ignition phase of ignition. Their study identified multiple ignition and extinction modes as a function of kernel motion. Additionally, Yang et al.[11] analyzed flame kernel motion and demonstrated that lower local flow velocities and strain rates, coupled with longer residence times, significantly increased the probability of ignition. The present observations are consistent with these prior findings, reinforcing the notion that flow-kernel interactions—particularly those influenced by recirculation zones—are critical in determining ignition success.

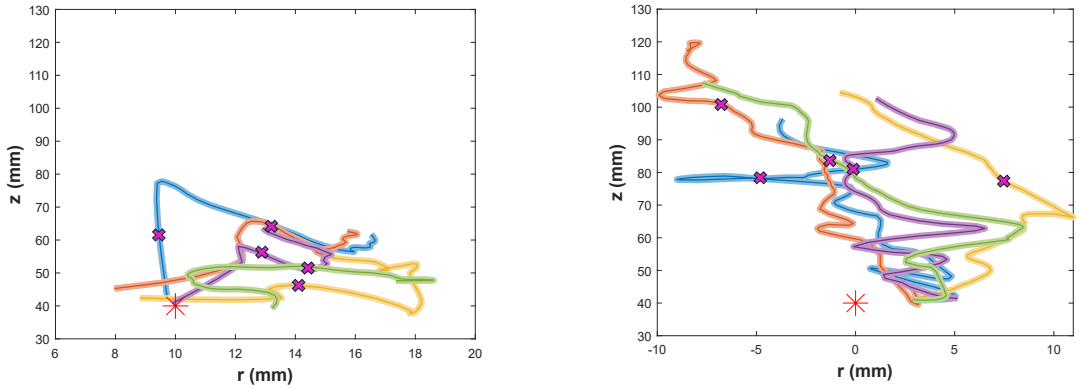

(a) (b)

Fig. 4.10 Kernel trajectories based on high-speed imaging for five iterations over a 8 ms duration following the laser spark, at (a) r = 10 mm, Ignition, (b) r = 0mm, Long-mode failure. Laser energy = 80 mJ. The nominal spark location is shown as red star at z = 40 mm. The kernel location at 5 ms is shown as magenta crosses.

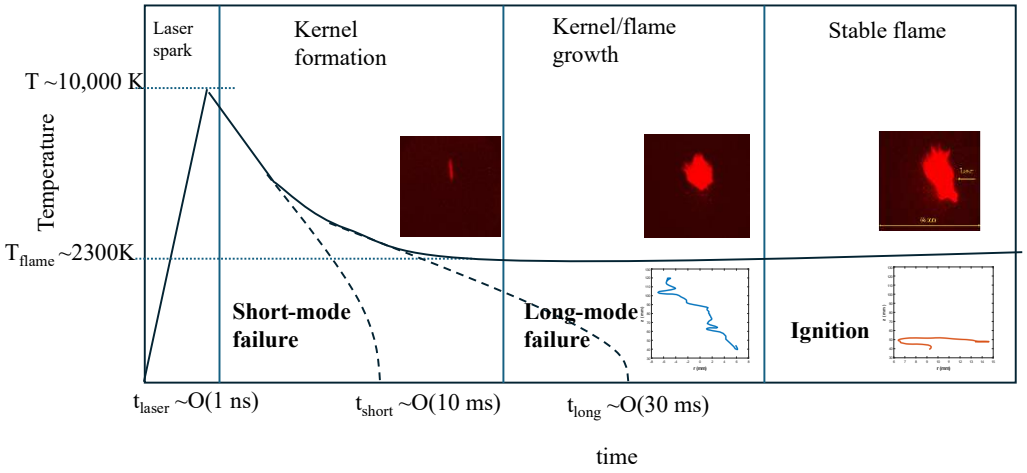

Fig. 4.11 Schematic illustrating the characteristic timescales and temperatures associated with short-mode failure, long-mode failure, and successful ignition. This schematic builds upon the qualitative framework proposed by Oliveira[3], providing a quantitative depiction of the ignition modes and includes the plasma temperature (typically ~10,000 K)[42] and adiabatic flame temperature of heptane (~2300 K) [37,43].

The schematic in Figure 4.11 summarizes the insights derived from the present study. Upon laser deposition in the spray, a high-temperature plasma is formed (typically ~10,000 K[42]). This plasma rapidly cools via recombination processes, typically within a few microseconds. If the deposited laser energy is too low, the resulting spark gives rise to a small flame kernel that extinguishes quickly—usually within 10 ms. Despite the high initial temperature, the quantity of reactive species generated under these conditions is insufficient to sustain combustion, resulting in a short-mode failure. At higher laser energies, the outcome depends on the ignition location and local flow conditions, and it can result in either a long-mode failure—where the flame kernel survives longer (~30 ms) before quenching—or successful ignition, where the kernel transitions into a stable flame. In successful cases, the post-recombination kernel temperature approaches the adiabatic flame temperature of heptane[36,43] enabling continuous combustion.

Two primary factors were identified as critical to ignition success: laser pulse energy and ignition location. While high-energy pulses (250 mJ) consistently resulted in successful ignition (with spray conditions under flammability limits), ignition was also achievable at moderate energies (80 mJ) when the ignition location was shifted to more favorable regions—typically near recirculation zones. These zones offer enhanced residence times, favorable velocity gradients, and improved entrainment of fresh reactants, all of which promote kernel growth and flame stabilization. In contrast, ignition near the burner centerline, where strong axial flows dominate, often resulted in flame kernel displacement and extinction, even at moderate energies. Overall, the evolution of a flame kernel into a self-sustained flame is governed by a complex interplay of factors, including incident energy, ignition location, and flow–kernel interactions. Local turbulence intensity, convective heat losses, and the ability of the kernel to entrain unburned reactants contribute to determining whether ignition is ultimately achieved.

CHAPTER 5: Conclusions

The objective of this research was to develop a deeper understanding of spray ignitability, with the ultimate goal of informing the design of more effective ignition systems. The investigation was structured into two complementary components. Chapter 3 focuses on the fundamental interaction between individual droplets and a laser, while Chapter 4 addresses ignition phenomena within a spray burner. This chapter summarizes the key findings from Chapters 3 and 4 and concludes by outlining directions for future research.

5.1 Summary

In Chapter 3, the influence of droplet size, laser energy, and their combined effects on droplet fragmentation and species composition during the laser irradiation of heptane droplets was investigated using an acoustic levitator. Shadowgraphy and spatially resolved Laser-Induced Breakdown Spectroscopy (LIBS) diagnostics were employed to achieve the research objectives. The experiments revealed that at higher energy densities (>~70 mJ/mm^3), designated as Regime 2, multiple breakdown events occurred near the droplet–air interface on both the illumination and shadow sides of the droplet. The corresponding LIBS spectra exhibited strong atomic emission lines of H_α, O, and N. In contrast, at lower energy densities (<~70 mJ/mm^3), referred to as Regime 1, only a single breakdown event was observed, characterized by spectra containing solely C_2 molecular bands with no detectable atomic lines. These results indicate that droplet breakup dynamics are strongly governed by the ratio of laser energy to droplet volume. At lower energy densities, the energy available per heptane molecule is insufficient to generate multiple plasma events, resulting in fewer breakdowns compared to higher energy conditions. This variation in energy distribution influences both the frequency of plasma breakdowns and the chemical

composition of the resulting species. These observations also offer potential insights into the phenomenon of multiple kernel formation in spray-ignited flames. While droplet lensing remains a widely accepted explanation, another plausible mechanism is that, following the formation of the initial kernel, residual laser energy—unabsorbed during the primary plasma formation—continues to propagate and induces additional, smaller breakdown events. Although the available energy is reduced, the formation of secondary breakdowns remains feasible due to the smaller droplet sizes typically present in sprays, which require less energy for plasma initiation.

Furthermore, the electron density and temperature under Regime 2 conditions were determined using Stark broadening of the H_α line and the Boltzmann plot method, respectively. It was found that the electron densities and temperatures in the droplet-induced plasma were comparable to those observed in air plasmas. However, while air plasmas exhibited minimal spatial variation in electron density along the plasma channel, droplet plasmas showed a localized increase in electron density near the center of the illumination side.

The measurements also suggest that the plasma effects persist up to 1 μs after breakdown. This finding implies that, in sprays, estimations of electron density and temperature based on the methods employed in this study could be significantly influenced by residual plasma effects and may largely reflect properties similar to those of an air plasma. Measurements at later times are not feasible due to rapid recombination of hydrogen and oxygen species, leading to insufficient signal-to-noise ratios for reliable application of Stark broadening and Boltzmann methods. Consequently, new diagnostic techniques, such as CARS or Rayleigh scattering, would be necessary to accurately measure the local temperature at later stages.

In Chapter 4, Laser-induced ignition experiments were conducted in an annular co-flow spray burner to investigate the ignition behavior and ignitability of a heptane–air spray. The first set of

experiments were conducted at fixed laser energy and varying radial ignition locations. The H_α/O ratio and kernel size and number were obtained using LIBS. Although the H_α/O ratio decreased with increasing radial distance from the burner—due to reduced fuel–air mixture availability—it showed no clear correlation with ignition success. Similarly, while a higher number of kernels were observed near the burner centerline due to increased droplet density and higher fuel availability, no consistent relationship was found between kernel number and ignition outcome. Though the total kernel size correlated to successful ignition cases, no significant spatial trends were identified in relation to ignition position. These observations suggest that relying solely on average H_α/O ratios and/or kernel statistics may be insufficient for predicting spray ignition behavior.

The schematic in Figure 4.11 summarizes the insights derived from the second set of experiments. Upon laser deposition in the spray a localized high-temperature plasma is formed. This plasma rapidly cools via recombination processes, typically within a few microseconds. If the deposited laser energy is too low (30 mJ), the resulting spark gives rise to a small flame kernel that extinguishes quickly (<10 ms). Despite the high initial temperature, the quantity of reactive species generated under these conditions is insufficient to sustain combustion, resulting in a short-mode failure. At higher laser energies (≥ 50mJ), the outcome depends on the ignition location and local flow conditions, and it can result in either a long-mode failure—where the flame kernel survives longer (>30 ms) before quenching—or successful ignition, where the kernel transitions into a stable flame. The long-mode failures produced substantial radical pools and exhibited signs of progressing chain-branching chemistry leading to flame front propagation but were ultimately quenched—likely due to the inability to reach an anchoring point leading to blowoff. In successful ignition cases, the post-recombination kernel temperature approaches the adiabatic flame

temperature of the fuel enabling continuous combustion. While high-energy pulses (250 mJ) consistently resulted in successful ignition (with spray conditions under flammability limits), ignition was also achievable at moderate energies (80 mJ) when the ignition location was shifted to more favorable regions—typically near recirculation zones. These zones offer enhanced residence times, favorable velocity gradients, and improved entrainment of fresh reactants, all of which promote kernel growth and flame stabilization. The results presented not only highlight the influence of ignition location but also provide a framework for identifying optimal spark sites—particularly relevant for practical systems like gas turbine combustors employing laser ignition.

5.2 Future work

The energy density metric developed in the droplet study can be further expanded into a more comprehensive dimensionless parameter that incorporates additional factors such as droplet composition, density, laser wavelength, and pulse width. Such a parameter could provide a more universal framework for predicting droplet fragmentation regimes across different experimental conditions. By capturing both fluid and laser properties, this metric could enable the determination of the laser energy and pulse characteristics necessary for achieving consistent and efficient ignition in sprays. Moreover, the data and trends presented in this work could serve to validate and refine models of aerosol behavior droplet breakdown [19], and ignition phenomena[36] offering a foundation for broader predictive modeling efforts.

Future studies in spray ignition can build on these findings by systematically varying spray characteristics—such as droplet number density, velocity, and size distribution—to assess their relative contributions to spray ignitability. Controlled parametric studies could help disentangle the complex interplay between physical spray properties, chemical kinetics, and flow-field

dynamics during ignition. Furthermore, extending ignition experiments to include a range of fuels with differing physical and chemical properties would provide valuable insights into how fuel-specific factors, such as volatility, molecular structure, and chemical reactivity, influence the ignition process. Together, these studies would advance the development of more robust ignition strategies for practical combustion systems, including engines and gas turbines.

References

1. Turns SR. *An Introduction to Combustion: Concepts and Applications*. McGraw-Hill; 2000. https://books.google.com/books?id=rzo8PgAACAAJ

2. Lefebvre A, Ballal D. *Gas Turbine Combustion: Alternative Fuels and Emissions*. 3rd ed. CRC Press; 2010.

3. Lefebvre A, Ballal D. *Ignition and Flame Quenching in Flowing Gaseous Mixtures*. Vol 357.; 1977. https://royalsocietypublishing.org/

4. de Oliveira PM, Sitte MP, Kotzagianni M, M Allison P, Mastorakos E. A laser-induced breakdown spectroscopy method to assess the stochasticity of plasma-flame transition in sprays. *Meas Sci Technol*. 2022;33(9). doi:10.1088/1361-6501/ac7436

5. de Oliveira PM, Mastorakos E. Mechanisms of flame propagation in jet fuel sprays as revealed by OH/fuel planar laser-induced fluorescence and OH* chemiluminescence. *Combust Flame*. 2019;206:308-321. doi:10.1016/j.combustflame.2019.05.005

6. Mastorakos E. Forced ignition of turbulent spray flames. *Proceedings of the Combustion Institute*. 2017;36(2):2367-2383. doi:10.1016/j.proci.2016.08.044

7. Ballal DR, Lefebvre AH. Ignition of liquid fuel sprays at subatmospheric pressures. *Combust Flame*. 1978;31:115-126. doi:https://doi.org/10.1016/0010-2180(78)90122-0

8. WEHE SD, and ASHGRIZ N. Ignition Probability and Absolute Minimum Ignition Energy in Fuel Sprays. *Combustion Science and Technology*. 1992;86(1-6):45-65. doi:10.1080/00102209208947187

9. Kawahara N, Tsuboi K, Tomita E. Laser-induced plasma generation and evolution in a transient spray. *Opt Express*. 2014;22(S1):A44-A52. doi:10.1364/OE.22.000A44

10. Beduneau JL, Kawahara N, Nakayama T, Tomita E, Ikeda Y. Laser-induced radical generation and evolution to a self-sustaining flame. *Combust Flame*. 2009;156(3):642-656. doi:10.1016/j.combustflame.2008.09.013

11. Marchione T, Ahmed SF, Mastorakos E. Ignition of turbulent swirling n-heptane spray flames using single and multiple sparks. *Combust Flame*. 2009;156(1):166-180. doi:10.1016/j.combustflame.2008.10.003

12. Yang S, Zhang C, Lin Y, Xue X, Gan X. Experimental investigation of the ignition process in a separated dual-swirl spray flame. *Combust Flame*. 2020;219:161-177. doi:10.1016/j.combustflame.2020.05.010

13. Klein AL, Bouwhuis W, Visser CW, et al. Drop Shaping by Laser-Pulse Impact. *Phys Rev Appl*. 2015;3(4). doi:10.1103/PhysRevApplied.3.044018

14. Gelderblom H, Lhuissier H, Klein AL, et al. Drop deformation by laser-pulse impact. *J Fluid Mech*. 2016;794:676-699. doi:10.1017/jfm.2016.182

15. Rao DCK, Singh AP, Basu S. Laser-induced deformation and fragmentation of droplets in an array. *International Journal of Multiphase Flow*. 2022;148. doi:10.1016/j.ijmultiphaseflow.2021.103925

16. Avila SRG, Ohl CD. Fragmentation of acoustically levitating droplets by laser-induced cavitation bubbles. *J Fluid Mech*. 2016;805:551-576. doi:10.1017/jfm.2016.583

17. Avila SRG, Ohl CD. Cavitation-induced fragmentation of an acoustically-levitated droplet. In: *Journal of Physics: Conference Series*. Vol 656. Institute of Physics Publishing; 2015. doi:10.1088/1742-6596/656/1/012017

18. Gonzalez-Avila SR, Klaseboer E, Khoo BC, Ohl CD. Cavitation bubble dynamics in a liquid gap of variable height. *J Fluid Mech*. 2011;682:241-260. doi:10.1017/jfm.2011.212

19. Bulat P V., Minin OP, Volkov KN. Numerical simulation of optical breakdown in a liquid droplet induced by a laser pulse. *Acta Astronaut*. 2018;150:162-171. doi:10.1016/j.actaastro.2017.11.029

20. Hsieh WF, Eickmans JH, Chang RK. *Internal and External Laser-Induced Avalanche Breakdown of Single Droplets in an Argon Atmosphere*. Vol 4.; 1987.

21. Eickmans JH, Hsieh WF, Chang RK. *Plasma Spectroscopy of H, Li, and Na in Plumes Resulting from Laser-Induced Droplet Explosion*.; 1987.

22. Biswas A, Latifi H, Shah P, Radziemski LJ, Armstrong RL. *Time-Resolved Spectroscopy of Plasmas Initiated on Single, Levitated Aerosol Droplets*. Vol 12.; 1987.

23. Young A, Graham WG, Morgan TJ, Hüwel L. Laser-induced breakdown in liquid water: Influence of repeated laser pulses on plasma formation and emission. *J Appl Phys*. 2021;129(18). doi:10.1063/5.0044471

24. Helfman D, Litwinowicz S, Meng S, Morgan TJ, Hüwel L. Spatial, spectral, and temporal properties of laser-induced plasma in air near an aqueous solution and comparison with ambient air. *J Appl Phys*. 2023;133(18). doi:10.1063/5.0146676

25. Kennedy PK, Hammer DX, Rockwell BA. *LASER-INDUCED BREAKDOWN IN AQUEOUS MEDIA*. Vol 21.; 1997.

26. Lazic V, Colao F, Fantoni R, Spizzicchino V. Laser-induced breakdown spectroscopy in water: Improvement of the detection threshold by signal processing. In: *Spectrochimica Acta - Part B Atomic Spectroscopy*. Vol 60. ; 2005:1002-1013. doi:10.1016/j.sab.2005.06.007

27. Biasiori-Poulanges L, El-Rabii H. Shock-induced cavitation and wavefront analysis inside a water droplet. *Physics of Fluids*. 2021;33(9):097104. doi:10.1063/5.0063827

28. Jagadale VS, Rao DCK, Deshmukh D, Hanstorp D, Mishra YN. Modes of atomization in biofuel droplets induced by a focused laser pulse. *Fuel*. 2022;315:123190. doi:https://doi.org/10.1016/j.fuel.2022.123190

29. Eickmans JH, Hsieh WF, Chang RK. Laser-induced explosion of H2O droplets: spatially resolved spectra. *Opt Lett*. 1987;12(1):22-24. doi:10.1364/OL.12.000022

30. Jagadale VS, Deshmukh D, Hanstorp D, Mishra YN. Bubble dynamics and atomization of acoustically levitated diesel and biodiesel droplets using femtosecond laser pulses. *Sci Rep*. 2024;14(1). doi:10.1038/s41598-024-57802-8

31. Lewis B, von Elbe G. *Combustion, Flames and Explosions of Gases*. 3rd ed. Academic Press; 1987.

32. Weinberg F, Wilson JR. A preliminary investigation of the use of focused laser beams for minimum ignition energy studies. *Royal Society*. 1970;314(1517).

33. Phuoc TX. Laser-induced spark ignition fundamental and applications. *Opt Lasers Eng*. 2006;44(5):351-397. doi:10.1016/j.optlaseng.2005.03.008

34. Beduneau JL, Kim B, Zimmer L, Ikeda Y. Measurements of minimum ignition energy in premixed laminar methane/air flow by using laser induced spark. *Combust Flame*. 2003;132(4):653-665. doi:10.1016/S0010-2180(02)00536-9

35. Beduneau JL, Kawahara N, Nakayama T, Tomita E, Ikeda Y. Laser-induced radical generation and evolution to a self-sustaining flame. *Combust Flame*. 2009;156(3):642-656. doi:10.1016/j.combustflame.2008.09.013

36. Morgan CG. Laser-induced breakdown of gases. *Reports on Progress in Physics*. 1975;38(5):621. doi:10.1088/0034-4885/38/5/002

37. El-Rabii H, Zähringer K, ROLON JC, Lacas F. Laser ignition in a lean premixed prevaporized injector. *Combustion Science and Technology - COMBUST SCI TECHNOL*. 2004;176:1391-1417. doi:10.1080/00102200490473620

38. Reddy H, Abraham J. Ignition kernel development studies relevant to lean-burn natural-gas engines. *Fuel*. 2010;89(11):3262-3271. doi:https://doi.org/10.1016/j.fuel.2010.05.040

39. Kopecek H, Lackner M, Iskra K, et al. Laser ignition of methane-air mixtures at high pressures and optical diagnostics. *Proc SPIE*. 2003;5147:331-342. doi:10.1117/12.543678

40. Reddy H, Abraham J. Ignition kernel development studies relevant to lean-burn natural-gas engines. *Fuel*. 2010;89(11):3262-3271. doi:https://doi.org/10.1016/j.fuel.2010.05.040

41. Dumitrache C, Baumgardner M, Boissiere A, et al. A study of laser induced ignition of methane-air mixtures inside a Rapid Compression Machine. *Proceedings of the Combustion Institute*. 2017;36(3):3431-3439. doi:10.1016/j.proci.2016.05.033

42. Lee TW, Jain V, Kozola S. Measurements of minimum ignition energy by using laser sparks for hydrocarbon fuels in air: propane, dodecane, and jet-A fuel. *Combust Flame*. 2001;125(4):1320-1328. doi:https://doi.org/10.1016/S0010-2180(01)00248-6

43. Pavel N, Bärwinkel M, Heinz P, et al. Laser ignition - Spark plug development and application in reciprocating engines. *Prog Quantum Electron*. 2018;58:1-32. doi:10.1016/j.pquantelec.2018.04.001

44. de Oliveira PM, Allison PM, Mastorakos E. Ignition of uniform droplet-laden weakly turbulent flows following a laser spark. *Combust Flame*. 2019;199:387-400. doi:10.1016/j.combustflame.2018.10.009

45. Gebel GC, Mosbach T, Meier W, Aigner M. Optical and spectroscopic diagnostics of laser-induced air breakdown and kerosene spray ignition. *Combust Flame*. 2015;162(4):1599-1613. doi:https://doi.org/10.1016/j.combustflame.2014.11.024

46. Gebel GC, Mosbach T, Meier W, Aigner M, Le Brun S. An Experimental Investigation of Kerosene Droplet Breakup by Laser-Induced Blast Waves. *J Eng Gas Turbine Power*. 2013;135(2). doi:10.1115/1.4007776

47. Lee SH, Do H, Yoh JJ. Simultaneous optical ignition and spectroscopy of a two-phase spray flame. *Combust Flame*. 2016;165:334-345. doi:10.1016/j.combustflame.2015.12.016

48. Lokini P, Dumitrache C, Windom BC, Yalin AP. Simultaneous Laser Ignition and Laser-Induced Breakdown Spectroscopy of a Hydrocarbon Spray Flame. In: *AIAA AVIATION 2023 Forum*. AIAA AVIATION Forum. American Institute of Aeronautics and Astronautics; 2023. doi:doi:10.2514/6.2023-3603

49. Alsulami R, Windell B, Nates S, Wang W, Won SH, Windom B. Investigating the role of atomization on flame stability of liquid fuels in an annular spray burner. *Fuel*. 2020;265. doi:10.1016/j.fuel.2019.116945

50. Kotzagianni M, Yuan R, Mastorakos E, Couris S. Laser-induced breakdown spectroscopy measurements of mean mixture fraction in turbulent methane flames with a novel calibration scheme. *Combust Flame*. 2016;167:72-85. doi:https://doi.org/10.1016/j.combustflame.2016.02.025

51. Lawes M, Lee Y, Mokhtar AS, Woolley R. Laser Ignition of Iso-Octane Air Aerosols. *Combustion Science and Technology*. 2007;180(2):296-313. doi:10.1080/00102200701739198

52. El-Rabii H, Gaborel G, Lapios JP, Thévenin D, Rolon JC, Martin JP. Laser spark ignition of two-phase monodisperse mixtures. *Opt Commun*. 2005;256(4):495-506. doi:https://doi.org/10.1016/j.optcom.2005.06.058

53. El-Rabii H, Victorov SB, Yalin AP. Properties of an air plasma generated by ultraviolet nanosecond laser pulses. *J Phys D Appl Phys*. 2009;42(7). doi:10.1088/0022-3727/42/7/075203

54. Lokini P, Dumitrache C, Windom BC, Yalin AP. Laser-Induced Breakdown Spectroscopy and Shadowgraphy of Acoustically Levitated Heptane Droplets. *Photonics*. 2024;11(11). doi:10.3390/photonics11111044

55. Windom BC, Diwakar PK, Hahn DW. Dual-pulse Laser Induced Breakdown Spectroscopy for analysis of gaseous and aerosol systems: Plasma-analyte interactions. *Spectrochim Acta Part B At Spectrosc*. 2006;61(7):788-796. doi:https://doi.org/10.1016/j.sab.2006.06.003

56. Diwakar PK, Loper KH, Matiaske AM, Hahn DavidW. Laser-induced breakdown spectroscopy for analysis of micro and nanoparticles. *J Anal At Spectrom*. 2012;27(7):1110-1119. doi:10.1039/C2JA30012E

57. hahnLIBs.

58. Herdin G, Klausner DIJ, Martin DI, et al. *International Combustion Engine Devision Fall Technical Conference GE JENBACHER`S UPDATE ON LASER IGNITED ENGINES*. https://proceedings.asmedigitalcollection.asme.org

59. Raizer IUP (IUrii P. *Laser-Induced Discharge Phenomena / Yu. P. Raizer ; Translated from Russian by Albin Tybulewicz ; Edited by George C. Vlases and Z. Adam Pietrzyk*. Consultants Bureau; 1977.

60. Ostrovskaya G v, Zaĭdel' AN. Laser spark in gases. *Soviet Physics Uspekhi*. 1974;16(6):834-855. doi:10.1070/pu1974v016n06abeh004094

61. Ronney PD. Laser versus conventional ignition of flames. *Optical Engineering*. 1994;33(2):510-521. doi:10.1117/12.152237

62. Adelgren R, Elliot G, Knight D, Zheltovodov A, Beutner T. Energy deposition in supersonic flows. In: *39th Aerospace Sciences Meeting and Exhibit*. Aerospace Sciences Meetings. American Institute of Aeronautics and Astronautics; 2001. doi:doi:10.2514/6.2001-885

63. Dumitrache C, Limbach CM, Yalin AP. Threshold characteristics of ultraviolet and near infrared nanosecond laser induced plasmas. *Phys Plasmas*. 2016;23(9):093515. doi:10.1063/1.4963248

64. Dumitrache C, Vanosdol R, Limbach CM, Yalin AP. Control of Early Flame Kernel Growth by Multi-Wavelength Laser Pulses for Enhanced Ignition. *Sci Rep*. 2017;7(1). doi:10.1038/s41598-017-10457-0

65. Miziolek AW, Palleschi V, Schechter I. *Laser Induced Breakdown Spectroscopy*. Cambridge University Press; 2006. doi:DOI: 10.1017/CBO9780511541261

66. Lokini P, Dumitrache C, Windom B, Yalin AP. Plasma Parameters of Laser Irradiated Hydrocarbon Droplets in Air. In: *AIAA SCITECH 2024 Forum*. AIAA SciTech Forum. American Institute of Aeronautics and Astronautics; 2024. doi:doi:10.2514/6.2024-0401

67. Marzo A, Barnes A, Drinkwater BW. TinyLev: A multi-emitter single-axis acoustic levitator. *Review of Scientific Instruments*. 2017;88(8). doi:10.1063/1.4989995

68. Hasegawa K, Abe Y, Kaneko A, Yamamoto Y, Aoki K. Visualization Measurement of Streaming Flows Associated with a Single-Acoustic Levitator. *Microgravity Sci Technol*. 2009;21(1):9-14. doi:10.1007/s12217-009-9134-8

69. Lokini P, Dumitrache C, Windom B, Yalin AP. Laser-Induced Fragmentation and Spectroscopy of Acoustically Levitated Hydrocarbon Droplets. In: *AIAA AVIATION*

FORUM AND ASCEND 2024. AIAA Aviation Forum and ASCEND co-located Conference Proceedings. American Institute of Aeronautics and Astronautics; 2024. doi:doi:10.2514/6.2024-3900

70. Marco A Gigosos, Valentín Cardeñoso. New plasma diagnosis tables of hydrogen Stark broadening including ion dynamics. *Journal of Physics B: Atomic, Molecular and Optical Physics*. 1996;29(20):4795. doi:10.1088/0953-4075/29/20/029

71. Gigosos MA, Gonzalez MA, Cardenoso V. Spectrochimica Acta Electronica Computer simulated Balmer-alpha,-beta and-gamma Stark line profiles for non-equilibrium plasmas diagnostics. *Spectrochimica Acta Part B*. 2003;58:1489-1504. doi:10.1016/S0584-8547Ž03.00097-1

72. Van Der Horst RM, Verreycken T, Van Veldhuizen EM, Bruggeman PJ. Time-resolved optical emission spectroscopy of nanosecond pulsed discharges in atmospheric-pressure N 2 and N 2/H 2O mixtures. *J Phys D Appl Phys*. 2012;45(34). doi:10.1088/0022-3727/45/34/345201

73. O'Haver T. A pragmatic introduction to signal processing. *University of Maryland at College Park*. Published online 1997.

74. Ferrari RL. Plasma Diagnostic Techniques . Edited by R. H. Huddlestone and S. L. Leonard. Academic Press, 1965, pp. 627, $19.50. *J Plasma Phys*. 1967;1:156-156. https://api.semanticscholar.org/CorpusID:119995338

75. Alsulami R, Windell B, Nates S, Wang W, Won SH, Windom B. Investigating the role of atomization on flame stability of liquid fuels in an annular spray burner. *Fuel*. 2020;265:116945. doi:https://doi.org/10.1016/j.fuel.2019.116945

76. Brieschenk S, O'Byrne S, Kleine H. Laser-induced plasma ignition studies in a model scramjet engine. *Combust Flame*. 2013;160(1):145-148. doi:https://doi.org/10.1016/j.combustflame.2012.08.011

77. Franc JP. *The Rayleigh-Plesset Equation: A Simple and Powerful Tool to Understand Various Aspects of Cavitation*.

78. Hsieh WF, Eickmans JH, Chang RK. *Internal and External Laser-Induced Avalanche Breakdown of Single Droplets in an Argon Atmosphere*. Vol 4.; 1987.

79. Kramida A, Ralchenko Y, Reader J. NIST Atomic Spectra Database. doi:https://doi.org/10.18434/T4W30F

80. Cremers DA, Radziemski LJ, Loree TR. Spectrochemical Analysis of Liquids Using the Laser Spark. *Appl Spectrosc*. 1984;38(5):721-729. doi:10.1366/0003702844555034

81. Albrecht H, Hohmann H, Grunwald R. *On the Generation of C 2-Radicals by IR-Multiple-Photon Dissociation*.

82. Glumac N, Elliott G, Boguszko M. Temporal and Spatial Evolution of the Thermal Structure of a Laser Spark in Air. In: *43rd AIAA Aerospace Sciences Meeting and Exhibit*. Aerospace Sciences Meetings. American Institute of Aeronautics and Astronautics; 2005. doi:doi:10.2514/6.2005-204

83. Luo YR, Pacey PD. *Effects of Alkyl Substitution on Ionization Energies of Alkanes and Haloalkanes and on Heats of Formation of Their Molecular Cations Part 2.* Alkanes and Chloro-, Bromo-and Iodoalkanes*. Vol 112.; 1992.

84. Trickl T, Cromwell EF, Lee YT, Kung AH. State-selective ionization of nitrogen in the X 2Σ+gv+=0 and v+=1 states by two-color (1+ 1) photon excitation near threshold. *J Chem Phys*. 1989;91(10):6006-6012. doi:10.1063/1.457417

85. Tonkyn RG, Winniczek JW, White MG. *ROTATIONALLY RESOLVED PHOTOIONIZATION OF 0; NEAR THRESHOLD*. Vol 164.; 1989.

86. Kelley AP, Jomaas G, Law CK. Critical radius for sustained propagation of spark-ignited spherical flames. *Combust Flame*. 2009;156(5):1006-1013. doi:10.1016/j.combustflame.2008.12.005

87. He L, Guo Q, Gong Y, Wang F, Yu G. Investigation of OH* chemiluminescence and heat release in laminar methane–oxygen co-flow diffusion flames. *Combust Flame*. 2019;201:12-22. doi:https://doi.org/10.1016/j.combustflame.2018.12.009

88. Do H, Carter CD, Liu Q, et al. Simultaneous gas density and fuel concentration measurements in a supersonic combustor using laser induced breakdown. *Proceedings of the Combustion Institute*. 2015;35(2):2155-2162. doi:10.1016/j.proci.2014.07.043

89. Ferioli F, Buckley SG. Measurements of hydrocarbons using laser-induced breakdown spectroscopy. *Combust Flame*. 2006;144(3):435-447. doi:https://doi.org/10.1016/j.combustflame.2005.08.005

90. Stavropoulos P, Michalakou A, Skevis G, Couris S. Laser-induced breakdown spectroscopy as an analytical tool for equivalence ratio measurement in methane–air premixed flames. *Spectrochim Acta Part B At Spectrosc*. 2005;60(7):1092-1097. doi:https://doi.org/10.1016/j.sab.2005.03.021

91. Stavropoulos P, Michalakou A, Skevis G, Couris S. Quantitative local equivalence ratio determination in laminar premixed methane–air flames by laser induced breakdown spectroscopy (LIBS). *Chem Phys Lett*. 2005;404(4):309-314. doi:https://doi.org/10.1016/j.cplett.2005.01.105

92. Bengtsson PE, Aldén M. Optical investigation of laser-produced C2 in premixed sooty ethylene flames. *Combust Flame*. 1990;80(3):322-328. doi:https://doi.org/10.1016/0010-2180(90)90108-4

93. Marrero-Santiago J, Collin-Bastiani F, Riber E, Cabot G, Cuenot B, Renou B. On the mechanisms of flame kernel extinction or survival during aeronautical ignition sequences: Experimental and numerical analysis. *Combust Flame*. 2020;222:70-84. doi:10.1016/j.combustflame.2020.08.021